The Oxidation Behavior of a Selection of South African Chromites

Stefan Swanepoel[1, 2], Andrie M. Garbers-Craig[2,*] & Johan P. R. De Villiers[2]

[1]Samancor Chrome, Cullinan Place, Morningside, Sandton, Johannesburg, 2196, South Africa

[2]Centre for Pyrometallurgy, Department of Materials Science and Metallurgical Engineering, University of Pretoria, Pretoria, 0002, South Africa

*Correspondence to Andrie M. Garbers-Craig. Email: Andrie.Garbers-Craig@up.ac.za

Abstract

Fifteen commercial concentrates that are consumed in ferrochrome pre-oxidative sintering pelletizer operations were characterized, and exposed to oxidative roasting environments. Significant variance was found in the thermogravimetric behavior of the ores, which was observed to be strongly correlated with the starting Cr:Al ratio of the spinel ($r = 0.84$, $P < 0.001$). The formation of the sesquioxide phase during roasting was studied through comprehensive XRD and SEM–EDS analysis. Counter-diffusion of Mg^{2+} and Fe^{2+} cations with only limited diffusion of Cr^{3+} and Al^{3+} was observed. The final mass fraction of sesquioxide present after conversion was determined by calculations using SEM–EDS analyses and was found to be between 35 and 54 pct after oxidation at 1200 °C for 5 minutes. The mass fraction of sesquioxide was found to be most strongly correlated with the total Fe content of the starting chromite spinel ($r = 0.93$, $P < 0.001$). The sesquioxide phase that forms was confirmed to be a solid solution between Al_2O_3–Cr_2O_3–Fe_2O_3 with no evidence of pure hematite (Fe_2O_3) or eskolaite (Cr_2O_3) precipitate found.

Introduction

Ferrochrome (FeCr) is a critical raw material for the production of stainless steel, with 60 to 70 pct of the chromium (Cr) units required to produce stainless steel globally being virgin Cr supplied by FeCr[1] of which more than 90 pct is classified as high-carbon ferrochrome (HC FeCr).[2] The only economically viable Cr-containing raw material for the production of ferrochrome is chromite ore,[3] which is mined and beneficiated mainly in South Africa, India, and Kazakhstan.
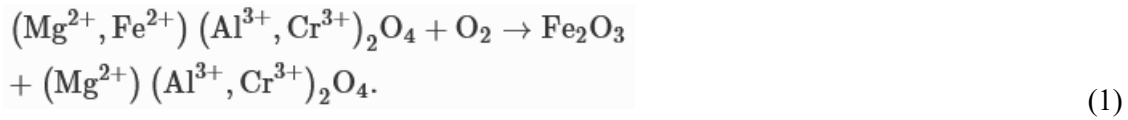
HC FeCr is predominantly produced in submerged arc furnaces (SAFs), where the liquidus temperatures for FeCr alloy and the typical operating slags formed require operating temperatures in excess of 1600 °C to facilitate efficient separation of the alloy and slag.[4,5] Although the energy consumption for HC FeCr production can be as high as 4.3 MWh/t FeCr, this can be nearly halved through a combination of pre-treatment processes.[6,7]

One such pre-treatment technology is the oxidative sintering of pelletized chromite concentrate, colloquially referred to as pre-oxidation[8] and commercially known as the steel belt sintering process, SBS.[9,10,11] It seems counterintuitive to pre-oxidize chromite ore, since the overall aim of smelting is to remove oxygen through carbonaceous reduction. The metallurgical benefits, however, have been well documented and include a lower specific
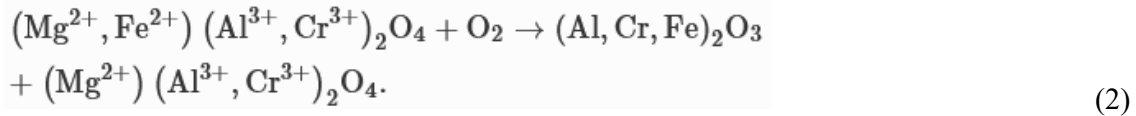
energy consumption and improved ore utilization.[12] The SBS process is in fact well adopted, to the extent that the current authors estimate at least 80 pct of the operational HC FeCr furnaces in South Africa utilized pre-oxidized chromite pellets at the time of writing. SBS pellets therefore play an important role in mitigating energy consumption in the South African ferrochrome industry.

The reason why pre-oxidation has a beneficial impact on subsequent SAF smelting relates to the crystal structure of the ore, which warrants some consideration. Normal spinel crystals have the general formula $(A^{2+})[B^{3+}]_2O_4$ with square brackets indicating octahedral sites and round brackets indicating tetrahedral sites.[13] The mineral chromite is such a cubic spinel and therefore has the chemical formula $FeCr_2O_4$.[14] Chromite ore, however, is not pure chromite but rather consists of a complex solid solution phase with the general form $(Mg, Fe^{2+})[Cr, Al, Fe^{3+}]_2O_4$.[15] Chromium cations are distributed throughout the crystal lattice, and solid-state reduction of these cations can only take place through complex ionic diffusion.[16]

The only cation present in chromite spinel that can be oxidized in air is the Fe^{2+}, which typically occupies tetrahedral sites. During oxidation, Fe^{2+} in the crystal lattice is oxidized to Fe^{3+}, which is more readily accommodated in octahedral sites.[17] Early works[18,19] suggest that the oxidation reaction resulted in 'splitting' of the spinel by precipitating Fe_2O_3. The oxidation products for full oxidation would then be hematite (Fe_2O_3) and a Fe-poor spinel after the unbalanced chemical reaction:

$$\left(Mg^{2+}, Fe^{2+}\right)\left(Al^{3+}, Cr^{3+}\right)_2O_4 + O_2 \rightarrow Fe_2O_3$$
$$+ \left(Mg^{2+}\right)\left(Al^{3+}, Cr^{3+}\right)_2O_4.$$

(1)

Detailed examination using XRD of the products after oxidation,[20,21] however, indicated that the sesquioxide phase that formed was not pure hematite but rather a R_2O_3 sesquioxide solid solution phase (where $R = Al^{3+}$, Cr^{3+}, Fe^{3+}). The chemical reaction for full oxidation would then rather be approximated by the unbalanced reaction:

$$\left(Mg^{2+}, Fe^{2+}\right)\left(Al^{3+}, Cr^{3+}\right)_2O_4 + O_2 \rightarrow (Al, Cr, Fe)_2O_3$$
$$+ \left(Mg^{2+}\right)\left(Al^{3+}, Cr^{3+}\right)_2O_4.$$

(2)

The R_2O_3 sesquioxide phase is found to precipitate in a typical Widmanstätten pattern[22] along the {111} planes of the spinel matrix phase and has been observed to result in Fe and Mg segregation between the two product phases.[23] This effectively increases the active surface area for reduction by breaking up the spinel particles into sub-grains, resulting in a beneficial impact on the reducibility of the chromite.[24]

A second reason that pre-oxidation is advantageous to the SAF relates to the reducibility of Fe cations to the reducing agents present. When considering the reduction reactions for iron oxides with varying oxidation states, it is revealed that iron oxides with higher oxidation states are thermodynamically more reducible with CO gas. The composition of $(Al, Cr, Fe)_2O_3$ that may form during oxidation can vary, which complicates consideration of the sesquioxide solid solution on the same graph, but the reducibility of Fe^{3+} in the sesquioxide solid solution is anticipated to be more favorable than that of $FeCr_2O_4$[25,26] while being less favorable than that of pure Fe_2O_3.[27]

A SAF provides a unique opportunity to exploit the increased reducibility by CO gas due to the counter-current movement of material and off-gas. In SAF production of HC FeCr, the off-gas typically contains 75 to 90 pct CO with temperatures ranging from 200 °C to 600 °C at the top of the burden where fresh feed is introduced.[28,29,30] As the material descends in the furnace the temperature it is exposed to increases to about 1600 °C just above the electrode tips but is expected to remain mostly solid burden up to 1200 °C.[31] A modified Baur–Glässner diagram that also considers the possibility of Fe_3C formation, as shown in Figure 1, indicates that partial $FeCr_2O_4$ reduction will not take place at temperatures below 1000 °C but confirms that the CO reducibility for iron oxides improves for higher oxidation states of iron. Feeding pre-oxidized chromite ore is therefore likely to allow for the utilization of gaseous reductant that would otherwise exit the furnace without having reacted. Although this does not account for kinetic limitations at lower temperatures, the mechanism of increased reduction by CO at low temperatures after pre-oxidation is confirmed by the fact that in practice solid carbon consumption used at the furnace does in fact not increase when feeding SBS pellets. The ability to feed pre-oxidized ore without increasing solid carbon requirements in the SAF through the use of CO in the off-gas for reduction was anticipated from the results of previous investigations.[32]
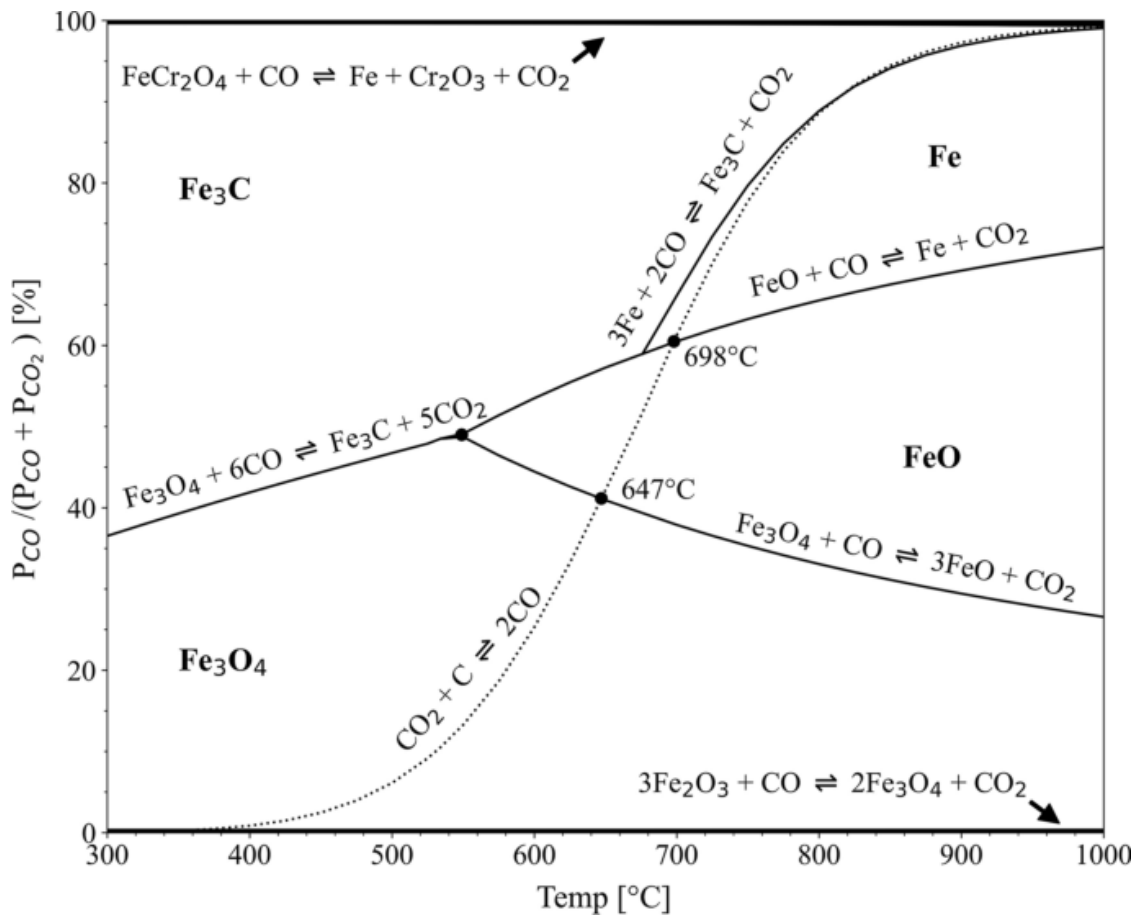

Fig. 1. Modified Baur–Glässner diagram constructed with data from FactSage8.0, assuming pure solids and 1 atm pressure

Considering the benefits discussed for using oxidized spinel as feed to a SAF, it stands to reason that optimizing the extent of oxidation would be beneficial to HC FeCr producers. In this work, the possible influence of the mineralogy of chromite ore is investigated. This work was in part

also motivated by industrial observations where, in contrast to past experiences, the performance of some industrial furnaces with increased pellet feed rates was found to be erratic. The expected improvement of 80 kWh/t for every 10 pct increase in pellet feed[33] was found to be only 52 kWh/t. Significant variability and unpredictability were also experienced, which was not observed at other furnaces during the same time period.

In South Africa, the chromite layers found in the Bushveld complex are divided into the lower group (LG), middle group (MG), and upper group (UG) layers, with varying composition between the layers.[34,35,36,37] Ore from a newly commissioned MG-seam mine was introduced to the SBS operation feeding the furnaces in question, while the remaining SBS operating parameters investigated were within normal operating limits for the site. Raw lumpy ore from the same seams, sized between 25 and 100 mm, was also fed to the furnaces previously and no adverse interaction with the slag regime or reductant mix was observed, that would have otherwise suggested that the fluxing regime in the furnace was incompatible with ores from the new seams. No information regarding the expected behavior of the MG-seam chromite during oxidation could be found during a literature study, and the information available for the LG and UG sourced materials did not provide enough clarity to allow for SBS process optimization of pre-oxidation rates.

Pre-oxidation of chromite has received an increasing amount of attention to lower production costs and as a result of an increasing global awareness of energy efficiency. Borra *et al.*[38] investigated the pre-oxidation of a single chromite ore from the Sukinda region in India between 800 and 900 °C, while Kapure *et al.*[39] exposed a single Indian chromite ore to an oxidizing environment at 900 °C. Biswas *et al.*[40] investigated the kinetics and phase transformations for two Indian chromite ores, confirming sesquioxide formation at 1000 °C.

Zhu *et al.*[41] compared the oxidation behavior of a high FeO South African chromite concentrate with that of a Chinese magnetite concentrate between 200 and 1000 °C. Additional work from the same group[25,42] investigated the consolidation and solid-state reduction behavior of pellets made from blends of chromite and magnetite roasted to a peak temperature of 1300 °C.

Kleynhans *et al.*[43] studied the pre-oxidation of a UG2 concentrate for use in an existing pre-reduction process, concluding that the pre-oxidation temperature needs to be restricted to below 1000 °C to prevent the formation of pure eskolaite (Cr_2O_3).

In none of these previous studies, the relationship of the chromite mineralogy as it relates to South African chromite concentrates which may originate from the LG, MG, or UG seams was considered as a variable. To optimize operational and economical parameters for a SBS–SAF operation, it is vital that the conditions for optimal oxidation are determined and understood.

The current work was initiated to expand on the understanding of the behavior of South African chromites during oxidative roasting, in the context of the change in operational behavior observed at the furnaces. It was decided to exclude the impact of the SBS variables (milled particle size distribution, bentonite addition, moisture content, pellet size, fluctuating temperature over the sinter belt cross section *etc.*), and rather investigate the behavior of the ores in their unagglomerated form.

Fifteen ores covering the MG, LG, and UG seams were sampled and characterized before and after being exposed to various oxidative roasting conditions. The aims of this investigation

were (a) to experimentally compare the extent of oxidation for the different ores at increasing temperature; (b) to experimentally examine the cation distribution after oxidation between the spinel and sesquioxide phase; (c) to examine the propensity, if any, for pure eskolaite exsolution above 1000 °C as this could have a passivating effect on subsequent reduction reactions; and (d) to determine whether any of the chromites were susceptible to oxidation at lower temperatures which would allow for oxidation technologies other than the SBS process to be considered.

Materials and Methods

Materials

Fifteen ore samples (samples A–O, Table I) were collected from ores that are supplied to SBS operations by sampling from dispatch stockpiles at the various mines from across the Eastern and Western Limb of the Bushveld Complex. As some mines actively mine multiple seams of a layer together (e.g., MG1 and MG2) and treat them simultaneously through a single beneficiation plant, the concentrate produced reflects a blended product and is indicated as such. No additional upgrading of materials was performed. One chemical-grade concentrate (Sample A)[44] and one foundry-grade concentrate (Sample I)[45] were included in the sampling as well as three unwashed 'chip' products (samples K, N, and O) originating from opencast mining activities. The remainder, and majority, of the samples were classified as metallurgical-grade concentrates.

The decision to use as-received ores for this study, without additional upgrading of the concentrate, was taken to replicate the behavior that the SBS plants are likely to experience. Removing the gangue components would also eliminate any low temperature interactions between the chromite and the gangue that could potentially influence the solid-state reactions observed in practice.

Methods

Sample preparation

Samples were dried in a drying oven at 105 °C for 24 hours after which the samples were milled to > 90 pct passing size of 212 μm.

Bulk chemical analysis

A wet chemical method using inductively coupled plasma optical emission spectrometry (ICP-OES) was used to perform chemical analysis of the major elements of the ores, reported as oxides with all Fe as FeO. A Spectro Arcos ICP-OES was used, calibrated against commercial chromite ore standards. The purpose of the ICP-OES analyses was to confirm that the elemental composition of the concentrates conformed to those of commercial concentrates, and that no undesirable elements were present.

Table I. Results of ICP-OES Analysis of Chrome Ore Samples

| Sample | Location | Seam | Product | ICP-OES Analysis (Mass Pct) | | | | | | | | | |
				Al_2O_3	CaO	Cr_2O_3	FeO	MgO	MnO	SiO_2	TiO_2	Total	Cr:Fe[1]
A	WL	MG1 and 2	chemical	14.87	0.15	44.07	25.92	9.35	0.22	1.70	0.73	97.03	1.50
B	EL	MG1 and 2	concentrate	15.43	1.07	39.01	24.58	10.21	0.21	7.15	0.77	98.45	1.40
C	EL	MG1	concentrate	14.12	0.59	42.53	24.69	10.00	0.22	3.87	0.60	96.65	1.52
D	WL	MG1 and 2	concentrate	13.89	0.89	36.84	23.38	11.17	0.21	9.45	0.65	96.52	1.39
E	EL	LG6, LG6a	concentrate	13.50	0.40	41.19	23.05	12.01	0.21	5.57	0.52	96.47	1.57
F	EL	MG0, 1, 2, 3	concentrate	14.11	0.57	42.07	24.48	10.12	0.22	4.24	0.57	96.41	1.51
G	EL	MG0, 1, 2, 3	concentrate	16.21	0.42	40.49	25.87	10.04	0.22	4.91	0.75	98.94	1.38
H	EL	MG0, 1, 2, 3	concentrate	16.14	0.58	39.33	25.22	9.74	0.21	4.91	0.71	96.88	1.37
I	WL	LG6	foundry	15.44	0.08	44.16	25.81	9.50	0.21	0.88	0.69	96.80	1.51
J	WL	UG2	concentrate	15.34	0.42	39.70	26.06	10.46	0.22	4.15	0.93	97.32	1.34
K	WL	LG5, LG6	chip	13.25	0.73	41.26	23.74	11.57	0.21	7.77	0.53	99.09	1.53
L	WL	MG3, 4	concentrate	17.62	0.37	40.14	25.29	9.82	0.21	3.63	0.73	97.84	1.40
M	WL	LG6	concentrate	15.29	0.36	42.65	24.78	10.65	0.21	4.54	0.64	99.15	1.51
N	EL	LG6	chip	12.72	0.52	38.96	21.96	12.81	0.20	9.40	0.53	97.14	1.56
O	EL	LG6	chip	13.04	0.39	40.05	22.56	12.06	0.20	7.46	0.55	96.33	1.56

WL, Western Limb of Bushveld; *EL*, Eastern Limb of Bushveld.
[1]Chromium to iron ratio calculated using the equivalent mass percentage of each element.

XRD analysis

Samples were prepared according to the standardized PANalytical backloading system, using circular sample holders. X-ray powder diffraction data, at room temperature, were collected on a PANalytical X'Pert Pro powder diffractometer in θ–θ configuration with an X'Celerator detector and variable divergence- and fixed receiving slits, equipped with Fe-filtered Co Kα radiation ($\lambda = 1.789$ Å). Samples were scanned from 5 to 90 deg, with a step size of 0.008 deg. Phase quantification and Rietveld refinement[46] were performed using Profex 4.3.2a.[47] R_{wp} (R-weighted pattern) values obtained varied between 2.25 and 4.06 pct across the raw and oxidized samples, which was deemed acceptable for this investigation. Additional chromite crystal structures used in the refinement were obtained from the Crystallography Open Database, COD[48] and the American Mineralogist Crystal Structure Database, AMCSD.[49] The XRD analyses were performed to confirm the mineralogical composition and crystalline structure of the ores, which is not routinely reported for commercial concentrates.

SEM analysis

ICP-OES and XRD analyses are not able to isolate the chromite crystals to the extent that a valence reconciliation allows for an accurate estimation of the oxidation state of Fe in the chromite crystals. Analyses of individual chromite particles were therefore performed by SEM–EDS to determine the cation composition of the chromite crystals more accurately. Samples for SEM analysis were cast in resin with the aid of vacuum impregnation and after polishing were sputter coated with gold for 60 seconds at 25 mA to achieve a coating of approximately 6 nm. Standardless energy-dispersive analysis of all phases was performed using a JEOL IT300 scanning electron microscope equipped with a XMAX50 Si-drifted EDS detector. Spectra were collected with 40 seconds of live time and 10 scans per phase were performed to allow for average elemental concentrations to be calculated. A working distance of 11 mm and accelerating voltage of 15 kV were used throughout to perform the analysis. To confirm the reliability of results obtained (specifically oxygen content), a sample of hematite powder (Merck, α-Fe$_2$O$_3$, 99.99 pct) was mounted using the same mounting and sputter coating techniques and analyzed. Deviations from the expected mass percentage values were 0.75 pct absolute and 1.1 pct relative and were considered acceptable for the purposes of the investigation.

Thermogravimetric analysis

Thermogravimetric (TG) analysis of individual ores was performed using a PerkinElmer STA 8000 thermal analyzer to evaluate oxidation behavior. The thermograms were recorded in air (flowrate 20 mL/min) with 300 mg of sample in alumina crucibles, at an isochronal heating rate of 10 °C/min up to 1150 °C. In addition, consecutive isothermal soaks in air (20 mL/min) were performed on three ores (sample E, sample J, and sample O) allowing 30-min holds each at 500 °C, 800 °C, 1000 °C, and 1200 °C, with isochronal heating of 10 °C/min applied between the hold temperatures.

Oxidation in a muffle furnace

To generate an adequate amount of oxidized sample for SEM and XRD examination, various roasting runs were performed in a temperature-controlled laboratory muffle furnace, using alumina refractory crucibles. For all the bulk oxidation runs, samples were heated in the furnace, in air, from ambient temperature at a rate of 10 °C/min up to the desired temperature

and then quenched in air, by removing them from the furnace, once the designated soak times were reached. The crucibles were weighed empty, with material before roasting and with material (2 to 3 g) after roasting using an analytical balance (with accuracy of 0.1 mg), and the percentage mass gain after roasting was calculated. The weight gain was measured to allow for reconciliation between these runs and the TG experiments.

Between three and five crucibles were loaded with a single ore type per run such that an average mass gain could be determined after roasting. Fourteen of the ores were treated at 800 °C for 4 hours and in separate runs with fresh sample at 1200 °C for 1 hour and for 4 hours, respectively. Three ores (designated sample E, sample J, and sample O) were selected for roasting in separate runs for 5 minutes and for 4 hours at a range of isothermal hold temperatures, namely, 500 °C, 600 °C, 700 °C, 800 °C, 1000 °C, and 1200 °C.

Thermodynamic modeling

FactSage8.0[50] was used to perform thermodynamic calculations using data from the FToxid (solution) and FactPS (pure substance) databases. The spinel solid solution model that is used in FactSage is well documented by Degterov *et al.*[51] It was developed within the framework of the compound energy formalism (CEF)[52] and was chosen as the preferred thermodynamic model to represent the solid-state spinel for this study.

Results

As will be discussed in Section III–B, the oxidation behavior of the fifteen concentrates was found to fall into one of three distinct groups. For the sake of brevity, only one from each group has been selected for discussion, to reflect the typical behavior of the entire group. Readers should please refer to the Electronic Supplementary Material (ESM) for the extended results of the remaining ores.

Raw Ore Characterization

Bulk chemical analysis

The results from the ICP-OES analysis are summarized in Table I, with the Cr_2O_3 content covering a wide range from 36.84 to 44.16 pct by mass. In addition to reflecting the substantial variation between chrome ores across the Bushveld complex, this also illustrates the wide range of concentrate products that are currently being produced. Historically, only concentrates with a 44 pct Cr_2O_3 content were produced, with a 42 pct Cr_2O_3 specification only becoming palatable when UG2 concentrate became more prolific in the traded chrome ore market. Although not commonplace, 38 pct Cr_2O_3 concentrates are also actively being produced by mines[53] and consumed by SBS plants.

XRD analysis

The major phase identified by Rietveld refinement of the X-ray diffraction data was chromite, with enstatite being the second most dominant phase identified as shown in Table II. Anorthite was present in significant quantities in some of the MG concentrates (samples B, D, G, and H), while smectite and talc were identified in two of the unwashed products (samples N and O). Sample D, which has a high anorthite content, also has a high talc content, and the combined

Table II. XRD Rietveld Refinement Results

Sample	Refinement Parameters			Phase Quantities (Mass Pct)					
	R_{exp} (Pct)	R_{wp} (Pct)	Lattice Parameter, a (Å)	Chromite	Enstatite[5]	Quartz[6]	Smectite[7]	Talc[8]	Anorthite[9]
A	2.27	2.83	8.304	95[1]	5	—	—	—	—
B	2.31	3.33	8.304	79[1]	8	—	—	—	14
C	2.25	3.29	8.303	90[1]	10	—	—	—	—
D	2.39	3.53	8.305	64[2]	9	—	—	16	12
E	2.32	3.16	8.303	84[1]	16	—	—	—	—
F	2.29	3.15	8.304	92[1]	8	1	—	—	—
G	2.28	3.17	8.298	85[1]	7	—	—	—	7
H	2.29	3.48	8.298	83[1]	7	—	—	—	10
I	2.26	3.13	8.299	100[1]		—	—	—	—
J	2.25	3.31	8.302	90[1]	10	—	—	—	—
K	2.49	4.28	8.303	82[1]	17	1	—	—	—
L	2.44	3.53	8.290	90[3]	10	—	—	—	—
N	2.54	5.54	8.294	67[4]	20	—	7	6	—
O	2.56	5.04	8.301	62[1]	23	1	11	3	—

[1] $(Fe^{2+}_{0.633}, Mg_{0.356}, Mn_{0.009}, Zn_{0.003})[Al_{0.622}, Fe^{3+}_{0.188}, Mg_{0.070}, Cr_{1.073}, Ni_{0.005}, Ti_{0.032}, V_{0.010}]O_4.$
[2] $(Fe^{2+}_{0.547}, Mg_{0.416}, Mn_{0.007})[Al_{0.679}, Fe^{3+}_{0.206}, Mg_{0.046}, Cr_{1.062}, Ni_{0.006}, Ti_{0.021}, V_{0.010}]O_4.$
[3] $(Fe^{2+}_{0.581}, Mg_{0.387}, Mn_{0.007})[Al_{0.724}, Fe^{3+}_{0.066}, Mg_{0.044}, Cr_{1.153}, Ni_{0.004}, Ti_{0.022}, V_{0.012}]O_4.$
[4] $(Fe^{2+}_{0.539}, Mg_{0.432}, Mn_{0.007})[Al_{0.601}, Fe^{3+}_{0.168}, Mg_{0.036}, Cr_{1.187}, Ni_{0.003}, Ti_{0.017}, V_{0.010}]O_4.$
[5] $MgSiO_3.$
[6] $SiO_2.$
[7] $H_1Al_2Ca_{0.5}O_{12}Si_4.$
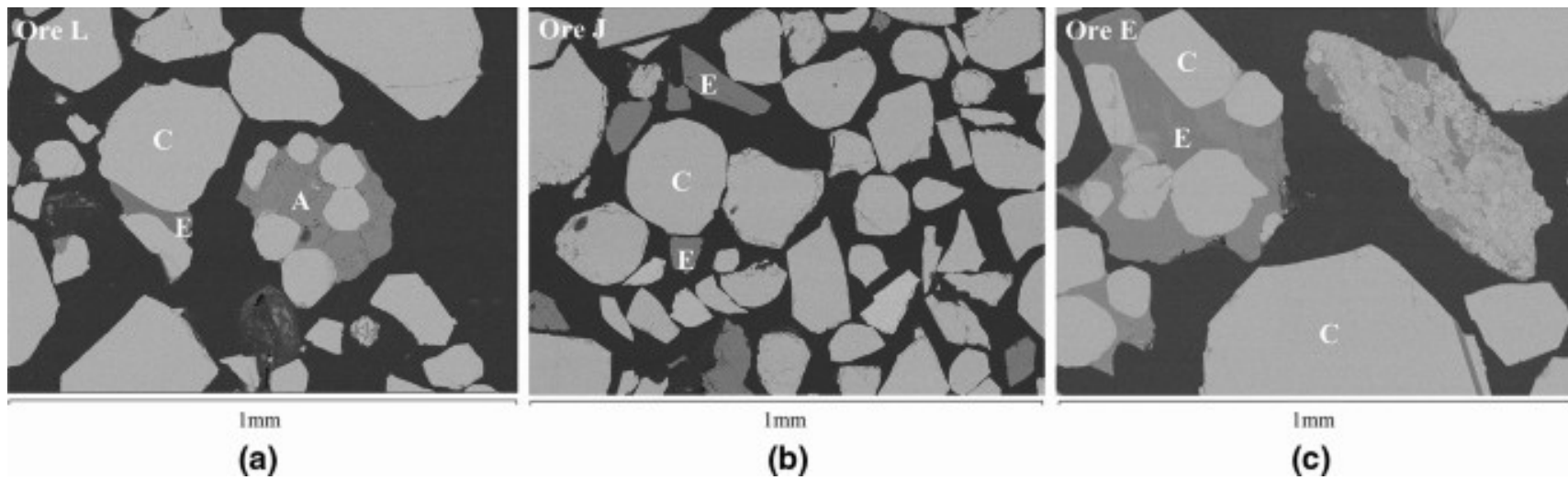[8] $Mg_3(OH)_2Si_4O_{10}.$
[9] $CaAl_2Si_2O_8.$

Fig. 2. Selected backscatter electron images for the as-received ores, (*a*) Ore L, (*b*) Ore J, and (*c*) Ore E. The chromite spinel crystals (C) are the lighter gray phase, while the silicate-based gangue phases, enstatite (E), and anorthite (A) are darker in color

high gangue component is reflected in the low pct Cr_2O_3 value obtained, determined from ICP analysis.

SEM analysis

Backscatter electron images for three of the sample ores are shown in Figure 2. It should be noted that the images were specifically selected to contrast chromite and gangue particles, and should not be considered representative of the relative amounts of gangue present. Although most of the chromite grains observed were large, euhedral, and well liberated, the SEM images for the MG-seam products also exposed unliberated chromite particles consisting of mixed chromite and pyroxene minerals. These 'chats' are challenging to remove using density-based mineral processing methods. As a result, concentrates with lower average pct Cr_2O_3 contents are produced when these seams are mined. Additional milling to fully liberate the chromite can be considered, but there is a trade-off due to the difficulty in recovering the ultra-fines (i.e., $< 25 \ \mu$m) that are generated in the milling process. This is demonstrated in Figure 2(b), which shows a UG2 concentrate which has been produced as a by-product from PGM mineral processing. Despite the improved liberation due to milling, gangue particles are still present in the chromite concentrate.

Chromite crystals are generally well liberated, but in Figures 2(a) and (c), we see evidence of smaller chromite grains encapsulated in silicate gangue that have not been liberated. Of the ores investigated, only Ore J has been subjected to milling during mineral processing, which does improve the liberation of the chromite grains as shown. The remaining ores were only crushed, and therefore, gangue particles are inevitably present in most chromite concentrates produced in South Africa. The exception to this being foundry-grade concentrates, since the size and shape requirements for foundry grains result in an ore from which chromite crystals are naturally liberated and readily upgraded.

The presence of these gangue contaminants in commercial concentrates implies that bulk chemical analysis is inadequate to fully characterize the mineralogical, oxidative, and smelting behavior of chromite concentrates. SEM–EDS, however, can be used to analyze the chromite spinel particles in isolation with the average EDS analysis for three of the chromite grains summarized in Table III (Table S-I in the ESM contains the results for the remaining ores).

Table III. Average Spinel Grain Compositions from EDS Analysis (Mass Pct)

	Ore E		Ore J		Ore O	
	Average	SD	Average	SD	Average	SD
Cr_2O_3	46.82	0.74	43.83	1.23	47.40	1.98
Al_2O_3	15.91	0.50	17.55	0.72	15.99	0.30
Fe_2O_3	8.31	0.24	7.80	0.14	7.82	0.19
FeO	17.12	0.49	20.06	0.36	17.85	0.43
MgO	11.29	0.21	10.20	0.21	10.94	0.21
TiO_2	0.09	0.29	0.92	0.50	0.08	0.25
Sum	99.53		100.36		100.08	
N	11		10		9	

N, number of EDS analyses performed.

Table IV. Molar Cation Proportions for Raw Ores Derived from SEM–EDS Analyses, Normalized to Four Oxygens Atoms

	Ore E		Ore J		Ore O	
	Average	SD	Average	SD	Average	SD
Cr	1.191	0.019	1.107	0.031	1.203	0.050
Σ Fe	0.662	0.019	0.724	0.013	0.668	0.016
Al	0.604	0.019	0.661	0.027	0.605	0.011
Mg	0.541	0.015	0.486	0.014	0.523	0.021
Ti	0.002	0.007	0.022	0.012	0.002	0.006
Sum	2.96		3.03		3.01	
N	11		10		9	
$X_{Fe^{2+}} = n_{Fe^{2+}}/\Sigma n_{Fe}$	0.70		0.74		0.72	
$n_{Cr}{:}n_{Al}$	1.97	0.064	1.68	0.056	1.99	0.096
$n_{Mg^{2+}} + n_{Fe^{2+}}$	1.00	0.034	1.02	0.032	1.00	0.043

N, number of EDS analyses performed.

The EDS results were used to calculate the spinel cation proportions and the oxidation state of the Fe cations as described by Droop,[54] with the results for three of the ores presented in Table IV, and Table S-II in the ESM containing same information for the remaining ores.

Thermogravimetric Analysis

Based on the ratio of divalent and trivalent Fe cations determined from EDS analysis, the calculated mass gain that can theoretically be achieved from full oxidation of the ores averages to 2.1 pct for the pure spinel grains. The gangue components present are, however, expected to predominantly experience mass loss in the region of 700 °C, typical behavior for the dehydroxylation of Fe-poor smectites,[55] the dehydration of talc,[56] or the dehydration of serpentine minerals.[57] Correcting for the dilution of chromite grains by gangue minerals as well as typical mass loss reactions, the expected change in the mass anticipated ranges from a mass loss of 1.3 pct for ores rich in clay to a mass gain of 2.2 pct for high chromite ores with high Fe^{2+} content. On average, a mass gain of 1.1 pct is anticipated. The experimental TG data for the ores fall within these ranges and are compared in Figure 3. The mass gain behavior could be classified into three distinct groups (Ore D was discarded due to its high gangue component and Ore H was excluded due to the similarity with the chromite collected from the neighboring mine, Ore G):
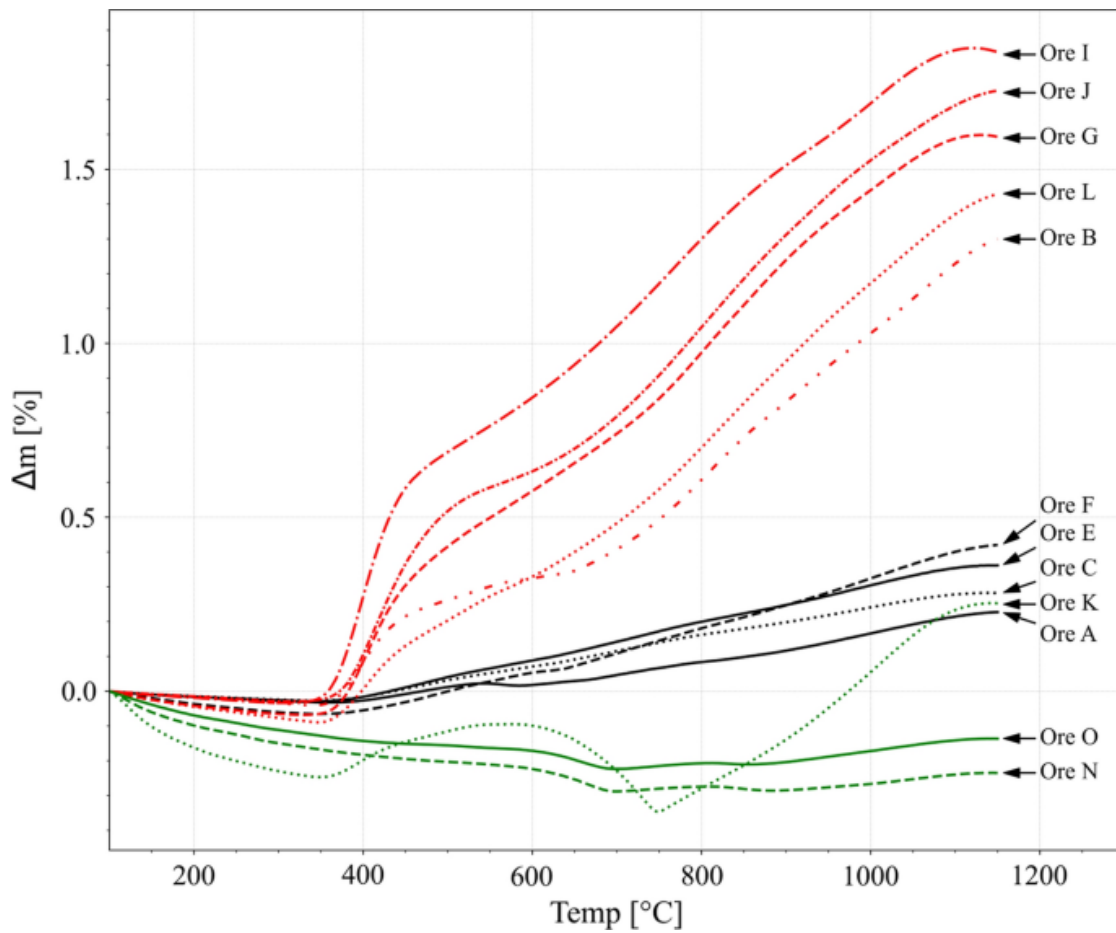

Fig. 3. TGA results for the as-received ores

Table IV. Molar Cation Proportions for Raw Ores Derived from SEM–EDS Analyses, Normalized to Four Oxygens Atoms

	Ore E		Ore J		Ore O	
	Average	SD	Average	SD	Average	SD
Cr	1.191	0.019	1.107	0.031	1.203	0.050
Σ Fe	0.662	0.019	0.724	0.013	0.668	0.016
Al	0.604	0.019	0.661	0.027	0.605	0.011
Mg	0.541	0.015	0.486	0.014	0.523	0.021
Ti	0.002	0.007	0.022	0.012	0.002	0.006
Sum	2.96		3.03		3.01	
N	11		10		9	
$X_{Fe^{2+}} = n_{Fe^{2+}}/\Sigma n_{Fe}$	0.70		0.74		0.72	
$n_{Cr}{:}n_{Al}$	1.97	0.064	1.68	0.056	1.99	0.096
$n_{Mg^{2+}} + n_{Fe^{2+}}$	1.00	0.034	1.02	0.032	1.00	0.043

N, number of EDS analyses performed.

Ores for which mass gain were initiated in the region of 350 °C, had varying oxidation rates between 350 °C and 600 °C, and then had similar rates of mass gain from 600 °C onwards, ultimately achieving between 1.3 and 1.84 pct mass gain (Ores B, G, L, I, and J, named Group 1).

Ores for which mass gain were also initiated around 350 °C but which had a significantly slower rate of oxidation than the first group, managing only to gain between 0.22 and 0.42 pct mass in total (Ores A, C, E, and F, named Group 2).

Ores which underwent net mass loss up to approximately 700 °C before any mass gain could be observed. Two ores in this group failed to achieve a net mass gain at the end of the heating profile (Ores O and N, named Group 3). The final one ore in this group (Ore K) achieved similar overall mass gain as observed in Group 2 despite the initial mass loss, recording a 0.25 pct mass gain. If the mass loss is accounted for such that the minimum mass recorded is at zero, the mass gain achieved after the initial mass loss is recalculated as 0.6 pct.

The mass loss observed in the ore from Group 3 could be attributed to the removal of water from the clay minerals, reflecting the unwashed nature of these products rather than the nature of the chromite spinel. Net mass loss reactions have been recorded for South African chromites previously in work done by MINTEK[58] as well as in an unpublished thesis[59] where mass change in air for South African chromites ranged from approximately -3.6 to $+2.2$ pct at 1200 °C. In these instances, the mass loss reactions could also be attributed to the presence of gangue minerals and mass gain to the oxidation of the Fe^{2+} in the spinel.

Other published work where oxidation of chromite was reported on using TG analysis shows results that are more closely aligned to that of the Group 1 ores, indicating that more than 1 pct mass gain at 1200 °C could be achieved.[23,41,60] The initiation of the mass gain step at around 350 °C, similar to the Group 1 and Group 2 chromites can also be observed.

The mass loss reactions observable for Group 3 from the onset up to 700 °C overlap with mass gain reactions for Groups 1 and 2 that initiates at 350 °C. The possibility of mass gain due to oxidation occurring concurrently with weight loss reactions suggests that the TG analysis alone could not be used to accurately calculate the extent of oxidation because the mass loss reactions could not be isolated. However, the consistency of the slopes observed on the oxidation curves above 600 °C suggests that the oxidation reaction was indeed dominant above 600 °C.
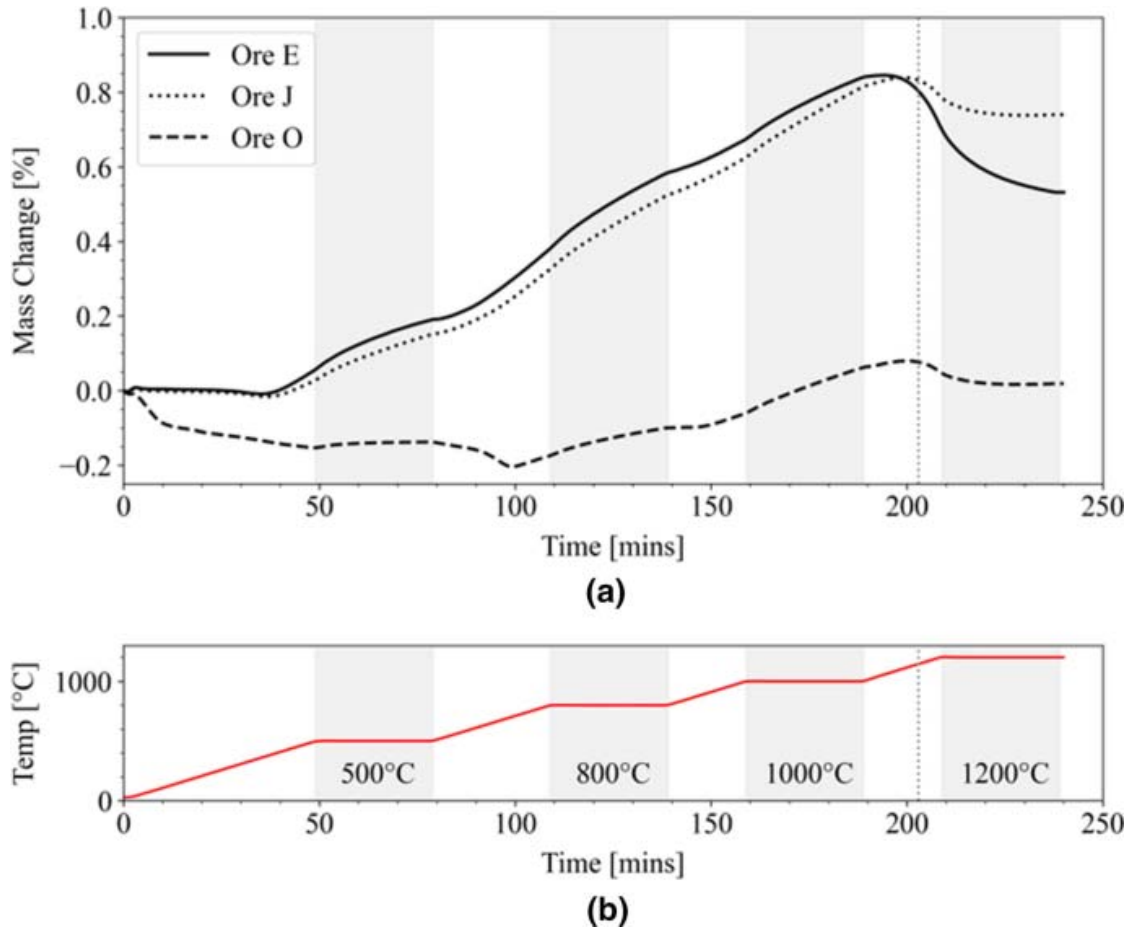
Fig. 4. TGA results for one ore from each of the initial groupings showing (*a*) the mass change during the experiment and (*b*) the temperature profile used. The shaded areas indicate the isothermal hold periods, and the vertical dashed line indicates a temperature of 1150 °C where the initial TGA runs were halted

To gauge the influence of mass loss reactions on the TGA results, one ore from each of the three groups identified during TG analysis was selected and subjected to TGA analysis with a hybrid temperature profile. The ores selected were Ores E, J, and O. In these tests, the samples were heated to 1200 °C but were held successively for 30 minutes at 500 °C, 800 °C, 1000 °C, and 1200 °C, respectively, to allow for slower reactions to occur and continue to a greater extent than the initial heating rate allowed for. In contrast to the previous results, with the new temperature profile, the two ores from Group 1 and Group 2 behaved similarly up to about 1100 °C (Figure 4). At higher temperatures, however, a mass loss step was observed which occurred at significantly different rates between the two ores which was not noticed in the initial TGA runs at 1150 °C. This mass loss step is attributed to the high temperature decomposition of the sesquioxide phase that formed during oxidation, similar to the decomposition of hematite that is observed at high temperatures according to[61]:

$$3Fe_2O_3 \rightarrow 2Fe_3O_4 + 0.5O_2. \tag{3}$$

It is unlikely that the solid product formed during this reaction step will be pure magnetite. Rather, it is expected that the product will instead form as a solid solution with spinel as this would result in a reduction of its activity, $a_{Fe_3O_4}$. Figure 5 demonstrates how the equilibrium oxygen partial pressure is anticipated to shift toward lower temperatures for the equilibrium

16

reaction as the activity of the solid product reduces. The decomposition temperature is therefore expected to vary across the chromite ores, considering the range of chromite spinel compositions and solid solutions that can form. In air at 1150 °C, it is calculated that Fe_2O_3 will decompose to magnetite when $a_{Fe_3O_4} = 0.014$.
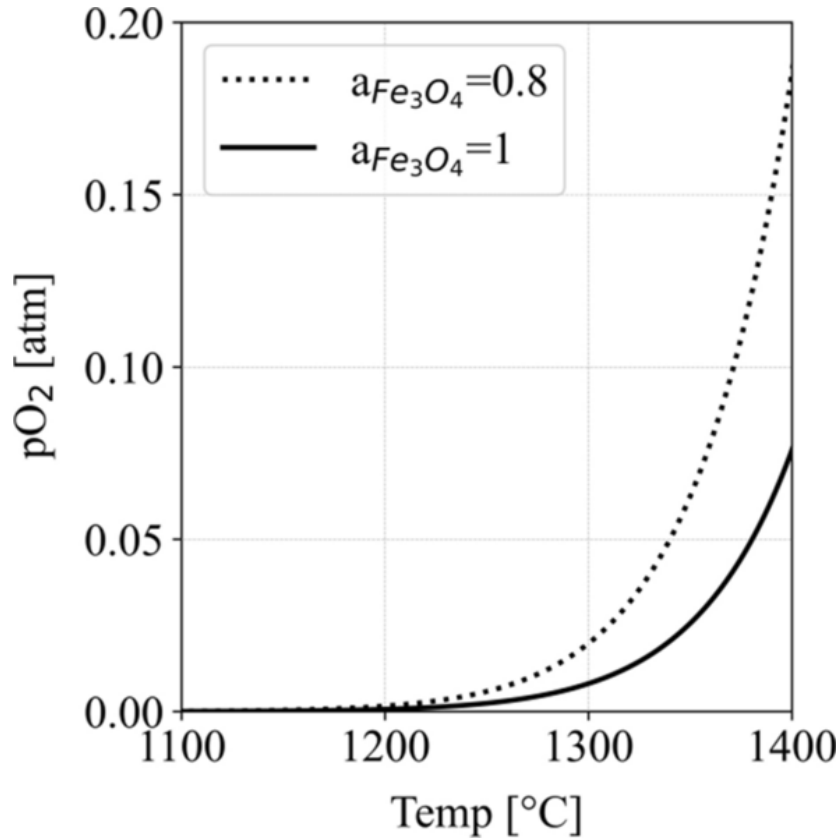
Fig. 5

Fig. 5. Temperature dependence of the equilibrium oxygen partial pressure for hematite decomposition with magnetite activity of 0.8 and 1 considered, with lower activity shifting the theoretical equilibrium conditions to lower temperatures (calculated using FactSage8.0)

It is interesting to note that Ores E and J experienced the same extent of mass gain in the isochronal section between 500 °C and 800 °C as was recorded for the 30 minutes hold at both 800 °C and 1000 °C (Table V). Together these three temperature stages account for 60 pct of the total mass gain, each accounting almost equally for around 20 pct of the mass gain. Holding for 30 minutes at 500 °C contributed about 15 pct of the mass gain with the isochronal stage from 800 to 1000 °C only accounting for about 10 pct of the overall mass gain for these two ores. Ore O only experienced net mass gain during the 30 minutes hold at 1000 °C, with approximately half of the mass gain observed taking place during this hold increment.

TGA results of Group 3 were again dominated by mass loss up to 700 °C with sesquioxide deoxidation above 1100 °C remaining a common observation across the three groups. Holding at 500 °C was found to be insufficient to allow the mass loss reactions to progress to completion. Upon further heating, mass loss re-initiated and reached a maximum at 700 °C before transitioning to a net mass gain reaction. From the start of the 800 °C hold up to the end

Table V. Incremental Percentage Mass Change for Each Stage of the Hybrid TG Runs Showing Similar Mass Changes for Ore E and Ore J Up to the End of the 1000 °C Hold Period, Before Divergent Mass Loss Increments Occur

Stage	Temperature Range	Ore E (Pct)	Ore J (Pct)	Ore O (Pct)
1	0 to 500 °C	0.06	0.03	− 0.15
2	30 minutes hold at 500 °C	0.13	0.12	0.02
3	500 °C to 800 °C	0.19	0.17	− 0.04
4	30 minutes hold at 800 °C	0.20	0.20	0.07
5	800 °C to 1000 °C	0.09	0.10	0.04
6	30 minutes hold 1000 °C	0.17	0.19	0.12
7	1000 °C to 1200 °C	− 0.14	− 0.03	− 0.02
8	30 minutes hold 1200 °C	− 0.17	− 0.04	− 0.03
	total Pct mass change	0.53	0.74	0.02

of the 1000 °C hold, Ore O experienced net mass gain but only approximately half of what the other two ores achieved over the same temperature range. The largest incremental mass gain for Ore O was when holding at 1000 °C, which contrasted with the other two ores, for which the largest mass gain event occurred when holding at 800 °C. Despite the influence of the gangue minerals at low temperatures on mass change, these results confirm the observations of the initial isochronal TGA runs which indicated that the oxidation behavior of the chromites is indeed distinct and unique.

Muffle Furnace Oxidation Runs

Several isothermal runs were performed in a muffle furnace at temperatures of 500 °C, 600 °C, 700 °C, 800 °C, 1000 °C, and 1200 °C, respectively. The samples were heated in air and held at the target temperature for 5 minutes during the initial run. For the second run of experiments, fresh sample was heated in air and held at the isothermal hold temperature for 4 hours. The 5-min sample runs were intended to approximate the TGA temperature profiles, with 5 minutes of soaking incorporated to allow for the sample to equilibrate with the furnace temperature. The time at peak temperature in the SBS process is estimated to be 10 minutes. A desktop study suggested that if longer retention times at similar temperatures were required, oxidative roasting in a rotary kiln would have to be considered over the SBS technology. Longer retention times would increase energy consumption due to increased thermal losses though, and a retention time of 4 hours was estimated to be the maximum retention time for which energy costs could be warranted by the benefits of pre-oxidation. Samples were prepared in triplicate such that average mass gain could be calculated.

These results are summarized in Figure 6 and agree with the TG results. For the experiments with a hold time of 5 minutes, mass gain for Ore E and Ore J was observed at low temperatures with incremental mass gain being observed for each incremental increase in hold temperature. At the highest temperature, both ores gained similar amounts of mass with Ore E gaining 1.60 pct and Ore J 1.84 pct. Ore O showed net mass loss during the lower temperatures for a 5-min hold that was essentially offset at 1000 °C, and only achieved a mass gain (0.62 pct) at 1200 °C. For all three ores, extended time of exposure to temperatures between 700 °C and 1000 °C led to an increase in mass gain (Table VI). The extent of mass gained from increased holding time was in most instances larger than the mass gain that was achieved by incremental increases in temperature. For all three ores, for example, essentially the same mass gain was observed at 1000 °C after 5 minutes as for 700 °C after 4 hours. This has significant implications for the technological considerations for pre-oxidizing chromite ores on industrial scale, *e.g.*, solar energy could be used as an energy source for low temperature oxidation technologies if adequate holding time at temperature is allowed for.

Table VI. Incremental Absolute Mass Change Incurred by Holding Samples for 4 Hours at Temperature Compared to the Mass Gain Achieved After 5 Minutes at Temperature

Hold Temperature (°C)	Ore E (Pct)	Ore J (Pct)	Ore O (Pct)
500	− 0.11	0.02	− 0.15
600	0.13	0.17	− 0.05
700	0.40	0.57	0.15
800	0.29	0.46	0.26
1000	0.50	0.40	0.51
1200	0.05	0.00	0.12

Table VII. Lattice Parameters for the Chromite Spinel and Sesquioxide Phases from Rietveld Refinement After Roasting at 1200 °C for 5 minutes

	R_{exp} (Pct)	R_{wp} (Pct)	Spinel Lattice Parameter a (Å)			Sesquioxide Lattice Parameters (Å)		Sesquioxide Mass Pct		
			Before	After	Pct Change (Pct)	a	c	XRD[1] (Pct)	SEM[2] (Pct)	FactSage[3] (Pct)
Ore E	2.36	3.72	8.303	8.290	− 0.20	4.960	13.512	32	35	43
Ore J	2.31	3.87	8.302	8.277	− 0.30	4.961	13.508	46	46	49
Ore O	2.33	3.68	8.301	8.292	− 0.10	4.959	13.510	28	36	45
Al_2O_3 (JPCDS PDF 10-173) Lattice Parameters	4.758	12.991								
Fe_2O_3 (JCPDS PDF 33-664) Lattice Parameters	5.036	13.749								
Cr_2O_3 (JCPDS PDF 38-1479) Lattice Parameters	4.958	13.593								

Estimated errors are smaller than the decimal precision reported for lattice parameters
[1]Normalised weight fraction between sesquioxide and spinel phase, excluding gangue phases
[2]Average area occupied by sesquioxide phase determined with ImageJ from SEM imaging, average of five measurements, area fraction taken to be equivalent to volume fraction. Average EDS composition used in conjunction with XRD lattice parameters to calculate theoretical crystal densities and convert the volume fraction occupied by sesquioxide to mass percentage
[3]Equilibrium phase composition calculated in air at 1200 °C with FactSage 8.0
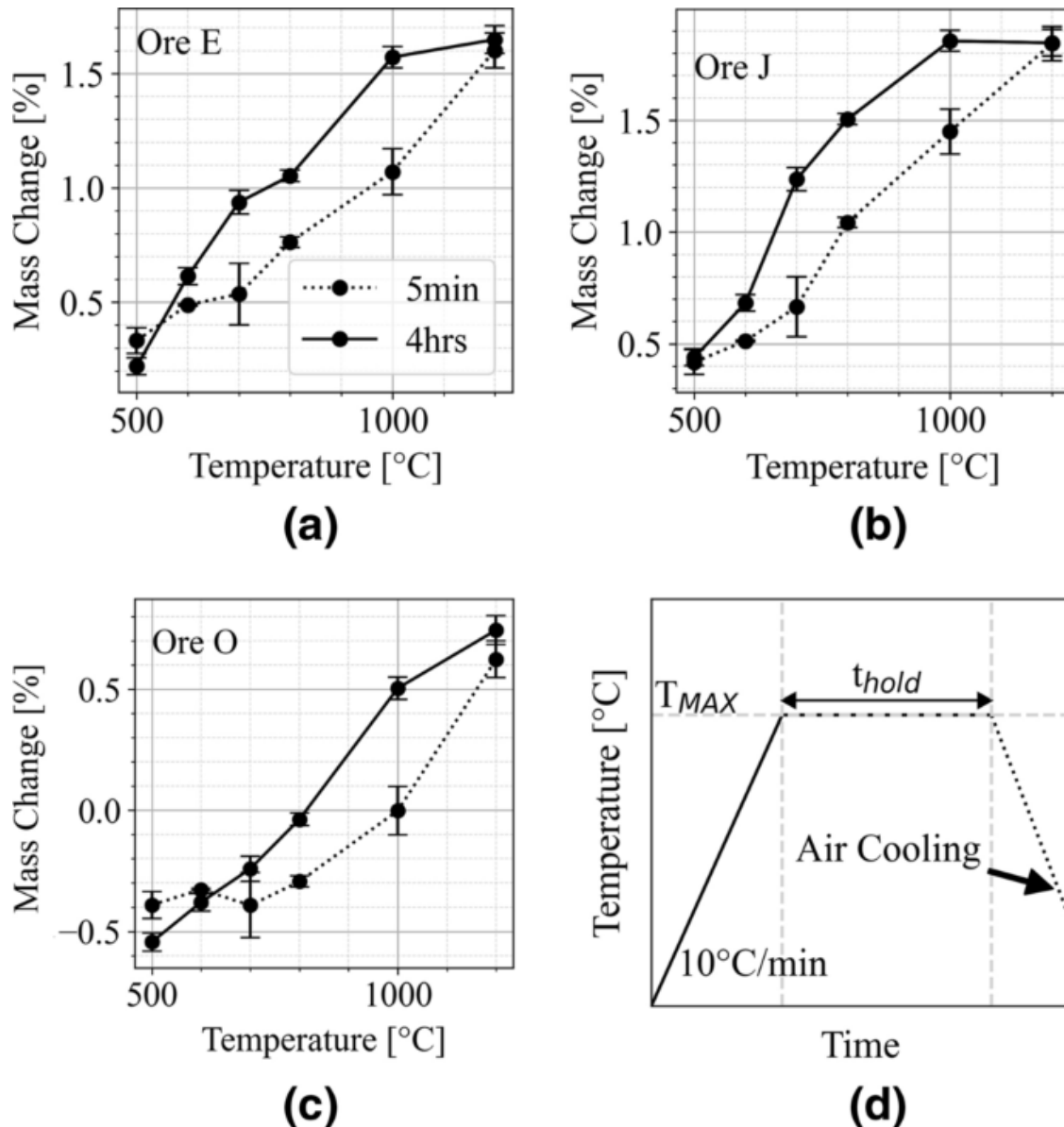
Fig. 6. Average mass changes recorded after bulk oxidation runs in a muffle furnace up to 1200 °C for (*a*) Ore E, (*b*) Ore J, and (*c*) Ore O, lines between datapoints are only added to guide the eye. (*d*) The setpoint temperature profile used

Where mass loss could be observed in the TGA results, no weight loss could be detected for the 5-min samples in the muffle furnace runs. For the 4-h samples, between 1000 °C and 1200 °C, a significant change in the slope of the percentage mass change *vs* temperature curves for all three ores was observed. Additionally, where the longer retention time at temperatures between 800 °C and 1000 °C led to an increase in mass gain, at 1200 °C a 5-min hold is equally as effective as a 4-h hold. Although this could be interpreted as an indication that equilibrium conditions have been reached after 5 minutes at 1200 °C, the weight loss observed in the TGA above 1000 °C should be considered, as a similar weight loss reaction might have been undetected in the muffle furnace runs. The final weight gain recorded after 4 hours at 1200 °C can therefore not be assumed to reflect the maximum mass gain achieved.

XRD Analysis

The XRD data for the ores after oxidation at 1200 °C for 5 minutes confirmed the formation of a new sesquioxide phase. The sesquioxide phase is anticipated to be a solid solution between Cr_2O_3–Fe_2O_3–Al_2O_3 that crystallizes with the corundum crystal structure. In all instances, a better fit was obtained during the Rietveld refinement when using an eskolaite crystal reference structure than when using that of hematite. However, care should be taken to interpret this as a positive identification of pure eskolaite, as there is a substantial amount of overlap in lattice parameters for solid solutions between these sesquioxides.[62,63,64] Such solid solutions are not commonplace, and powder diffraction databases are not likely to have reference patterns for the varying compositions, and as a result, one of the pure endmembers is likely to be identified as the closest fit. The lattice parameters for the altered spinels after roasting as well as both the lattice parameters for the sesquioxide phases are found to be strikingly consistent across all the chromites investigated (see Table VII). In all but one of the samples (Ore N in Table S-III in ESM), the chromite lattice was found to have contracted slightly after roasting.
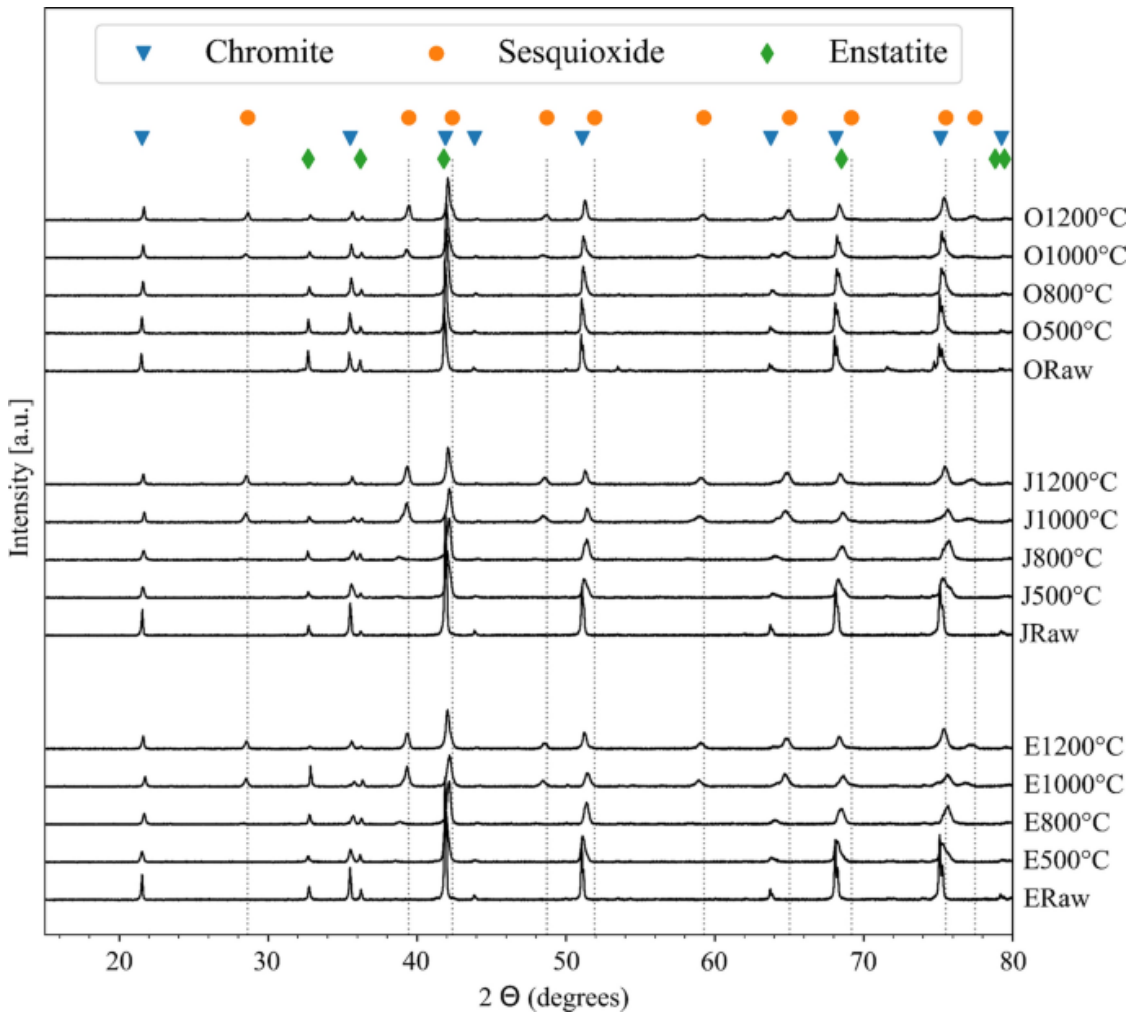

Fig. 7. XRD spectra for raw ores and after exposure to the indicated temperature for 5 minutes, with the presence of sesquioxide peaks only detectable after exposure to 800 °C

In Figure 7, the XRD spectra are shown for ores after roasting at different temperatures, demonstrating how the sesquioxide peaks appear and increase in intensity as the roasting temperature increases. Although new peaks are not as prominent after roasting at 500 °C, the shifts in the chromite peaks result in a sesquioxide phase being detected when performing Rietveld refinement. After roasting at 1200 °C, the sesquioxide phase that provided the best XRD spectra fit was eskolaite, while for the lower temperature roasts, hematite could also be fit as the sesquioxide phase to the observed XRD spectra to within acceptable refinement parameters, although this resulted in inferior fits to those achieved using eskolaite. Artificial powder diffraction patterns were also generated for the individual sesquioxide solid solutions using the lattice parameters as measured by XRD and the average EDS analysis for the phases. In all instances, superior Rietveld refinement results were again achieved using the eskolaite diffraction pattern as reference for the sesquioxide phase. Sesquioxide phase quantification was therefore executed using eskolaite as the reference pattern as reported in Table VII. The full comparison of results is given in Table S-III in ESM with XRD phase quantification indicating that the average mass of sesquioxide formed after oxidation was 40 pct. The highest mass percentage of sesquioxide formed, 47 pct, was achieved for sample D, while the lowest, 28 pct, was achieved for sample O.

SEM Analysis

A collection of SEM images of various chromite particles are included in Figure 8 for reference. Of particular interest was the presence of pores in the spinels that are not present in raw spinels. These are observed in individual particles after exposure to 800 °C, but become more prevalent across multiple particles at higher temperatures and longer exposure times. Longer exposure times tended to lead to a growth in the sesquioxide phase, leading to irregularly shaped edges, whereas the initial transformation had very sharply defined edges typical of the Widmanstätten lamellae.[65] Although an Fe-rich sesquioxide rim is observed around most oxidized chromite particles, the presence of the same sesquioxide phase in the cores of the particles did not appear to particularly proceed from the rim toward the center. Rather, when lamellae are present, they tend to be randomly distributed across the length of the chromite particles from the onset. As observed by Tathavakar *et al*.,[23] the precipitation appears to initiate as fine growths along one set of octahedral planes before transitioning to abundant growths along all sets of tetrahedral planes.

Evidence of oxidation at 500 °C could not unequivocally be observed with the SEM. However, an isolated number of particles were found that contained evidence of a secondary phase (Figure 8(e)). This phase, identified as darker in color in the electron backscatter images, was exclusively in the body of the chromite grains with no reaction products detectable in the rims of said particles. The scarcity and size of this phase did not allow for accurate identification using EDS. EDS analysis of the bulk chromite particles roasted at 500 °C for 4 hours did not indicate any detectable difference in composition and no increase in the trivalent iron content could be established.
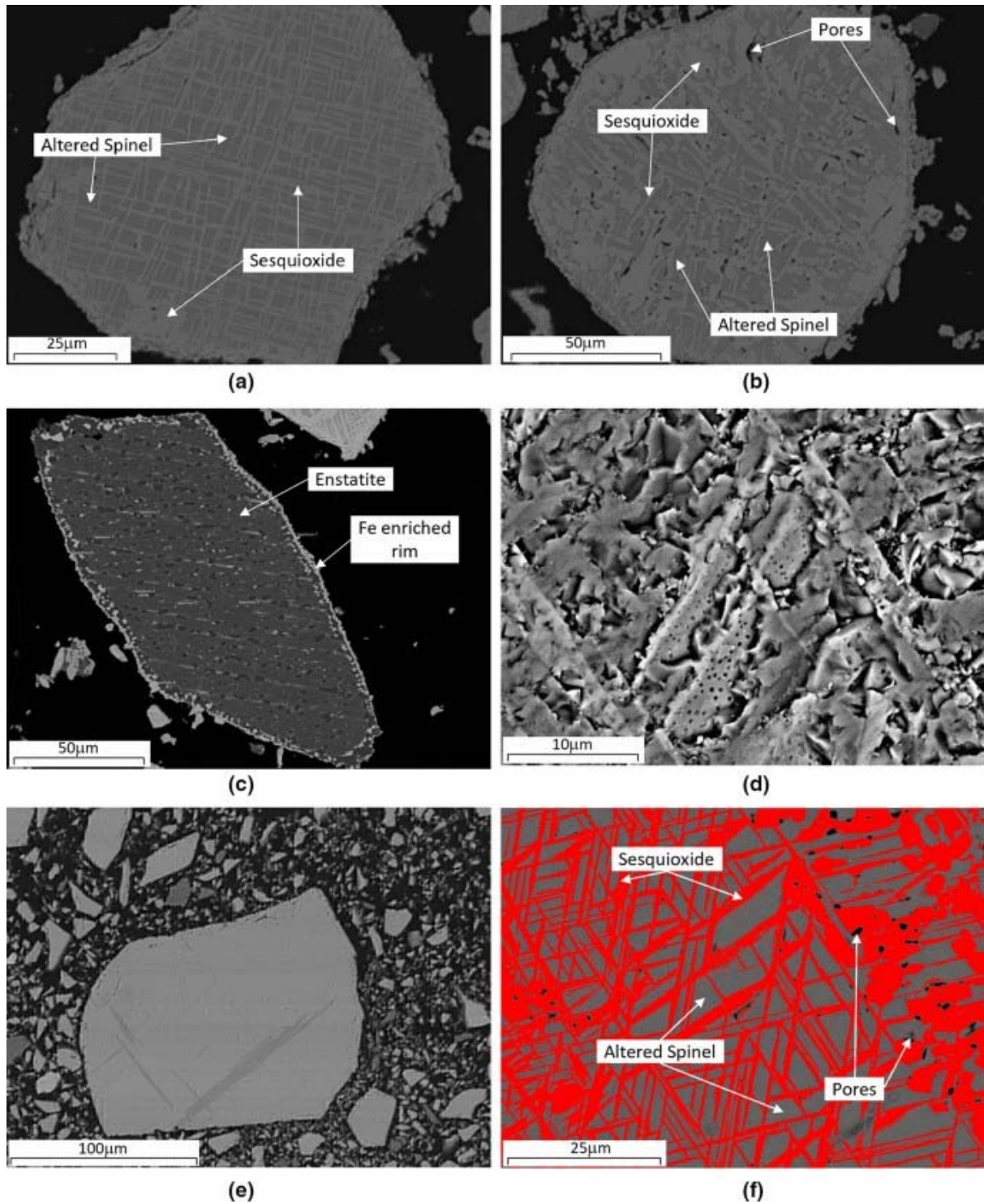
Fig. 8. A selection of backscatter electron images showing (*a*) a chromite particle with the lighter sesquioxide exsolved in a characteristic Widmanstätten pattern after 30 minutes exposure at 1200 °C with a few pores visible, (*b*) a chromite particle after exposure to 1200 °C for 4 hours, showing increased porosity and bleeding of the sesquioxide phase margins with significantly increased porosity, (*c*) a large enstatite gangue particle (dark color) which has been enriched in iron around the edges, (*d*) a secondary electron image of a roughly polished sample exposing circular pores in some of the sesquioxide lamellae, (*e*) a chromite particle after exposure to 500 °C with a secondary, darker, phase visible, and (*f*) example of how the ImageJ threshold adjustment was used to isolate and estimate the fraction of sesquioxide phase present

24

Enstatite particles were also found to be enriched in Fe on their periphery after roasting, with the boundary region toward the center of the particles being too thin to obtain accurate EDS analyses to confirm whether Fe depletion occurred adjacent to the area of enrichment. In instances where fusion between enstatite and chromite particles was observed, however, the enrichment in Fe was more apparent and the Fe-rich region visually thicker in the enstatite particles. This agrees with other researchers who found that when chromite ores are oxidized in the presence of magnesia rich silicates, the MgO present in the silicate matrix reacts rapidly with free sesquioxide to form a spinel structure.[66,67] Rigby et al.[68] reported similar diffusion of oxides from chrome grains into a silicate matrix when chrome ores were heated with a selection of silicates. Lekatou and Walker[22] sintered chromite briquettes containing silicate gangue in both air and argon, confirming that the formation of sesquioxide promotes diffusion between the chromite particles and gangue phases.

Image analysis was performed on the oxidized spinel particles using ImageJ v1.53e[69] to determine the area fraction occupied by the sesquioxide and the spinel phases. The average phase composition determined by EDS for the spinel and sesquioxide (Tables VIII and IX), as well as the lattice parameters obtained by the XRD analysis were used to calculate the theoretical densities of individual phases (full comparison between the remaining ores included in Tables S-IV and S-V in ESM). On the assumption that the area fraction observed is equal to the volume fractions observed in the samples, the mass fraction of each phase could be calculated using the theoretical phase densities. The calculated mass pct sesquioxide phase present for the individual ores is shown in Table VII, and while there is agreement with the XRD phase quantifications ($r = 0.66$, $P = 0.0102$), these calculated proportions were on average 4 pct higher than the XRD values. Figure 9 shows the cation compositions of the starting spinel with the two phases that form during oxidation. In all instances, the sesquioxide phase was enriched in Fe and almost depleted in Mg, with the altered spinel consequently being Mg enriched and reflecting a diminished Fe content. The molar ratio of Cr to Al cations, however, was found to be reasonably consistent across all three phases, indicating that only limited diffusion of these cations took place.
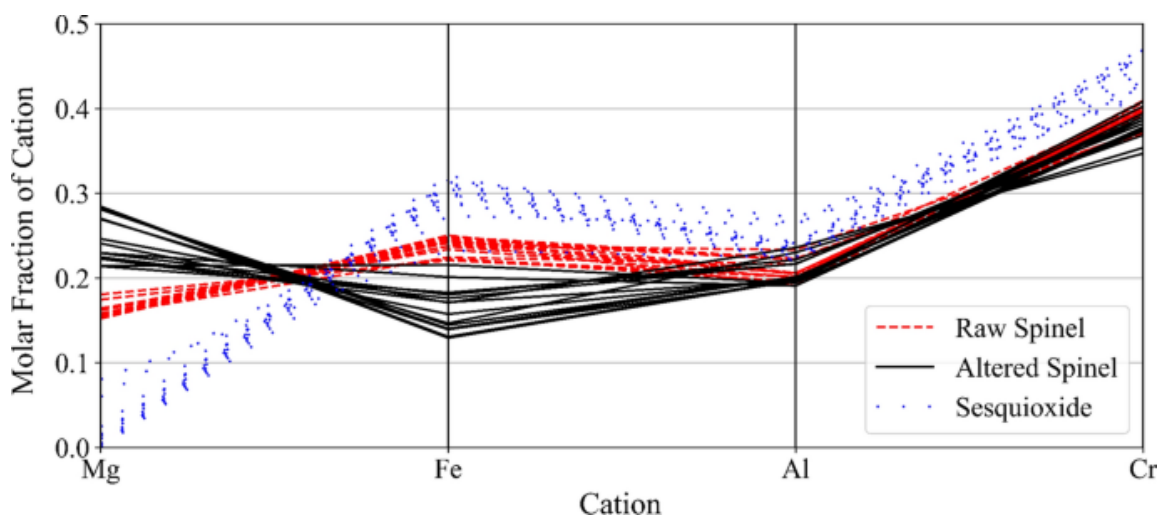

Fig. 9. Parallel plot showing the cation compositions of the oxidation products and the starting spinel as molar fractions for all the ores examined. The Cr:Al ratios remained stable as demonstrated by the parallel slopes between the Al and Cr categories, while Mg:Fe counter-diffusion is observed

Table VIII. Molar Cation Proportions for Oxidized Spinel Phase Derived from SEM–EDS Analyses, Normalized to Four Oxygen Atoms

	Ore E		Ore J		Ore O	
	Average	SD	Average	SD	Average	SD
Cr	1.159	0.013	1.134	0.108	1.107	0.02
Σ Fe	0.384	0.015	0.651	0.29	0.428	0.015
Al	0.585	0.011	0.586	0.063	0.595	0.016
Mg	0.839	0.02	0.647	0.241	0.832	0.016
Ti	0	0	0	0	0	0
Sum	2.967		3.018		2.963	
N	10		10		10	
$X_{Fe^{2+}} = n_{Fe^{2+}}/\Sigma n_{Fe}$	0.39		0.55		0.36	
Cr:Al	1.98	0.081	1.93	0.881	1.86	0.073
$n_{Mg^{2+}} + n_{Fe^{2+}}$	0.99	0.028	1.01	0.449	0.99	0.023

N, number of EDS analyses performed.

Table IX. Cation Proportions for Sesquioxide Phase Derived from SEM–EDS Analyses, Normalized to Three Oxygen Atoms

	Ore E		Ore J		Ore O	
	Average	SD	Average	SD	Average	SD
Cr	0.919	0.01	0.864	0.043	0.928	0.032
Al	0.466	0.015	0.445	0.033	0.475	0.024
Fe	0.609	0.023	0.585	0.088	0.568	0.032
Ti			0.006	0.013	0.004	0.013
Mg	0.003	0.008	0.12	0.142		
Sum	1.997		2.02		1.975	
N	10		10		10	
Cr:Al	1.97	0.065	1.94	0.174	1.96	0.12

Sesquioxidation

One of the earliest representations of chromite sesquioxidation was proposed by Rait[21] as part of an extensive study on the behavior of chromites from across the globe for use in refractory materials. In this approach, the spinel is represented as a solid solution of $RO \cdot R_2O_3$, with $RO = R_2O_3$ for a balanced spinel. As oxidation of the Fe^{2+} occurs, the RO ($n_{FeO} + n_{MgO}$) content diminishes, while the R_2O_3 ($n_{Fe_2O_3} + n_{Al_2O_3} + n_{Cr_2O_3}$) content increases. The newly formed R_2O_3 requires one RO molecule to form a spinel structure, without which it will form free sesquioxide. Mg^{2+} is the only cation remaining after full Fe oxidation to function as the RO unit in a spinel solid solution, and therefore determines the final amount of sesquioxide and altered spinel present. Using this proposed reaction mechanism, the molar quantity of free sesquioxide and altered spinel after oxidation can be calculated using the starting molar quantities:

$$n_{Altered\, Spinel\, after\, oxidation} = RO - n_{Fe^{2+}} = n_{Mg^{2+}}, \tag{4}$$

$$n_{Free\, Sesquioxide\, after\, oxidation} = R_2O_3 + 0.5 n_{Fe^{2+}} - n_{Mg^{2+}}, \tag{5}$$

where RO and R_2O_3 refer to the moles of divalent and trivalent oxides present in the unfired spinel. Using this method for Ore E, for example, predicts that after full oxidation, the mass fraction of sesquioxide phase will be 50 pct. This is significantly more than the 32 pct determined from Rietveld refinement and the 35 pct from the SEM area calculations. For the full set of ores analyzed, this calculation predicts 15 pct more sesquioxide phase by mass than experimentally determined *via* Rietveld refinement and 11 pct more than determined by the SEM area calculations. None of the ores were able to achieve the level of sesquioxidation predicted by the abovementioned mechanisms as shown in Figure 10.
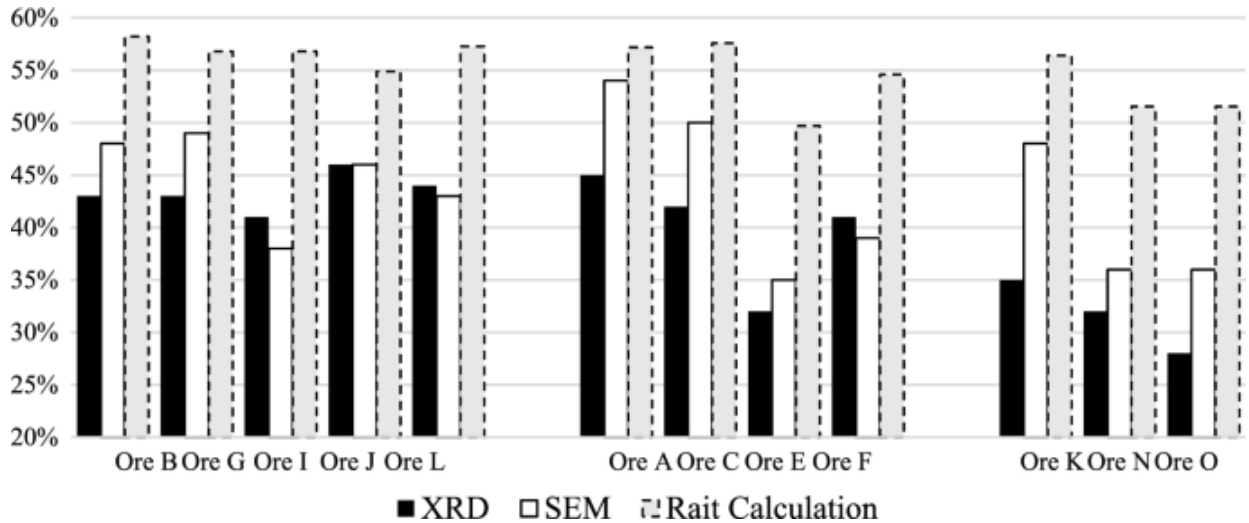

Fig. 10. Mass fraction of sesquioxide phase after oxidation at 1200 °C for 5 minutes as determined by Rietveld refinement, SEM area calculation, and the reaction mechanism proposed by Rait,[21] with experimental results being consistently lower

Thermodynamic data regarding the solid solubility between the three sesquioxide end members were limited at the time, and therefore, Rait[21] resorted to the assumption that the R_2O_3

constituents combine with RO in the same proportion in which these R_2O_3 components are present in the starting spinel. This assumption effectively fixes the molar ratios of Cr:Al, Al:Fe, and Cr:Fe in both the sesquioxide and altered spinel to the same ratios present in the starting spinel. Muan and Sömiya[70] experimentally confirmed that while a wide range of solid solutions are possible, a miscibility gap is present in the Fe_2O_3–Al_2O_3–Cr_2O_3 system in air between 1250 °C and 1500 °C. Particularly, in mixtures with a high Al_2O_3 content, Fe-rich and Al-rich sesquioxide phases were found to exist in equilibrium rather than a single sesquioxide phase. A more exact method than used by Rait[21] is required to predict the composition of the sesquioxide product formed during oxidation more accurately.

Equilibrium calculations using FactSage8.0, using the original spinel compositions determined with SEM–EDS, were used to calculate the equilibrium phase quantities and compositions from 400 °C to 1500 °C. A unique equilibrium composition was determined for each incremental temperature step with the original spinel composition as input, *i.e.*, products from one temperature increment did not carry over as feed to the next incremental temperature step. These results indicate that cation exchange is not likely to be limited to Fe and Mg but rather that Al and Cr redistribution is also expected to take place during oxidation. An example of the equilibrium results obtained for Ore E is shown in Figure 11, showing significantly better alignment with experimental results than the calculated values arrived at by using the approach by Rait[21] at 1200 °C. The calculated FactSage equilibrium sesquioxide mass percentages show superior correlation with SEM estimates ($r = 0.77$, $P = 0.001$) than with those determined by XRD ($r = 0.64$, $P = 0.0135$), and the FactSage sesquioxide phase estimates are on average 4.9 pct higher than the SEM estimates and 9 pct higher than the XRD estimates (see Table VII).
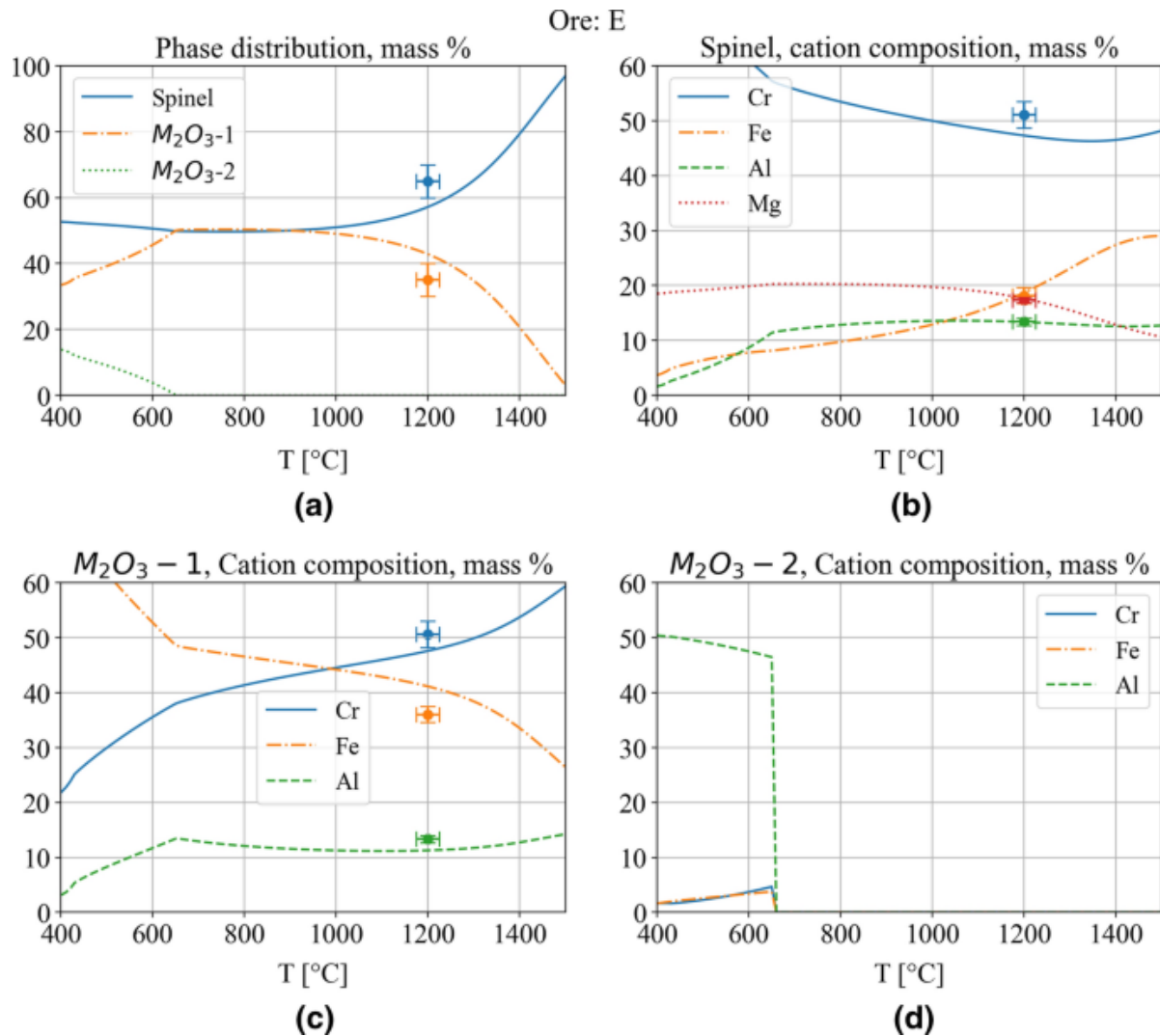
Fig. 11. Summary of results from equilibrium calculations done using FactSage8.0 for Ore E showing (*a*) the mass percentage of phases predicted to be present for increasing temperatures and experimental values calculated from SEM area calculations, (*b*) the average composition of the spinel phase as well as the average SEM–EDS compositions measured, (*c*) the composition of the primary sesquioxide phase with SEM–EDS compositions, and (*d*) the cation composition of a low temperature sesquioxide phase. Note that Mg is not predicted or detected in the sesquioxide phase and that FactSage predicts the formation of a second sesquioxide phase that disappears above 650 °C

As mentioned, thermodynamic data were limited during the Rait[21] investigation, and the ability of the sesquioxide phase to accommodate specific cations is expected to play a significant role in determining the final composition. Even at low temperatures, a solid solution between Cr_2O_3 and Fe_2O_3 is possible as shown in Figure 12, while a miscibility gap between Al_2O_3 and Fe_2O_3 is still present at 1300 °C. Also in Figure 12, the sesquioxide phase compositions determined by EDS after firing at 1200 °C are superimposed along with equilibrium compositions predicted using FactSage for the sesquioxide phase. Notably, complete solid solution is only possible between the two Cr_2O_3 and Fe_2O_3 end members at 600 °C. Complete solubility between the Al_2O_3 and Cr_2O_3 end members only occurs above 900 °C. Solubility between the Al_2O_3 and Fe_2O_3 end members remains limited even at 1300 °C. At higher temperatures, Fe_2O_3 decomposition takes place, leading to the formation of a spinel

phase that is not indicated on this diagram but causes continued immiscibility for low Cr_2O_3-containing mixtures. The simplification that Rait[21] used to estimate the final sesquioxide content after oxidation by assuming equal accommodation of Fe, Cr, and Al into the sesquioxide phase is therefore not supported thermodynamically. The implication of this is that at low temperatures, the sesquioxide solid- solution phase is not expected to accommodate Al, while Cr and Fe can be accommodated.
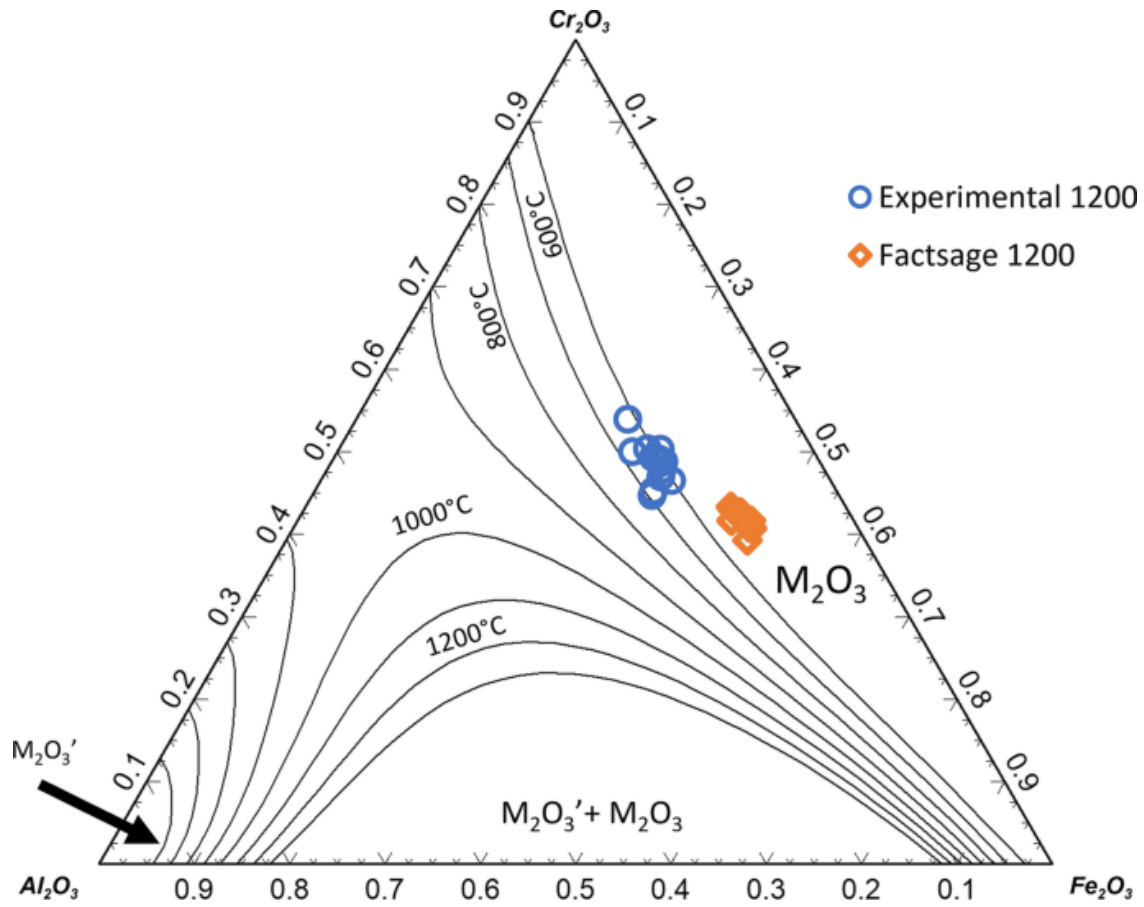

Fig. 12. Equilibrium ternary plots for the sesquioxide phase in air showing phase boundaries in 100 °C increments from 600 °C to 1300 °C, with compositions indicated as mass fractions

Due to the correlation with observed results, the FactSage equilibrium phase quantities are deemed to be a more realistic indication of the total amount of sesquioxide that can potentially form during oxidation. Equilibrium compositions of the sesquioxide phase calculated using FactSage are consistently higher in Fe content and lower in Cr and Al content when compared to experimental results. The normalized sesquioxide end member compositions for the experimental runs were also positioned close to where the sesquioxide phase boundary crosses the Cr:Al ratio lines of the raw ore, between 600 °C and 800 °C. This is also the same temperature range where sesquioxide diffraction peaks first became apparent and where mass gain was substantial. The deviation from the FactSage equilibrium calculations is not unexpected, since the duration of the experiments is likely too short to allow for equilibrium to be reached. Samples were also heated in air, with low temperature reaction products effectively becoming the feed products for higher temperature reactions, whereas the FactSage calculations performed assumed pure chromite spinel as feed at each temperature considered, ignoring the impact of reactions that may have occurred during heating.

In addition to thermodynamic stability, the diffusibility of individual cations also needs to be taken into consideration. Suzuki et al.[71] investigated diffusion coefficients in chromite spinels between 1400 °C and 1700 °C and at 3 to 7 GPa finding that Mg–Fe^{2+} diffusion is more than an order of magnitude faster than Cr–Al diffusion, and that Cr diffusion in turn is more than an order of magnitude slower than that of Al. Additionally, the diffusion rate of Mg–Fe^{2+} was found to be dependent on the Cr:Al ratio of the spinel which is in agreement with the stability of the Cr:Al ratio in the reaction products found in the present work. It is therefore argued that as divalent Fe diminishes during initial oxidation, the sesquioxide phase that forms from the decomposition of the spinel due to divalent cation loss has a Cr:Al ratio close to that of the parent spinel, due to the slow diffusion of both Cr and Al. The ability of this sesquioxide to accommodate additional Fe cations is then expected to correspond with the Cr:Al intersect of the sesquioxide phase boundary as was indeed found. Although not examined *in situ*, the increased porosity after oxidation indicates a physical separation between the sesquioxide phase and the altered spinel phase, which would naturally inhibit diffusion between the two phases as well.

To describe the average reaction behavior observed, minimization was performed using Microsoft Excel's Solver.[72] Firstly, a stoichiometric mass balance was set up for each of the ores using the average SEM–EDS compositions according to the general reaction:

$$\text{Spinel} + a(O_2) \rightarrow b\,(\text{Sesquioxide}) + c\,(\text{Altered}\backslash, \text{Spinel}),$$

(6)

where a, b, and c represent the stoichiometric coefficients needed to balance the reaction. The minimization function used was

$$f(X_i) = \sum_{j=1}^{70} (P_j - R_j)^2,$$

(7)

where P_j and R_j are the calculated number of moles of product and reagent elements, respectively. The elements considered for the 14 ores (excluding Ore M) were Fe, Mg, Al, Cr, and O. No error weighting was assigned, and the coefficients were set to vary between 0 and 3 and assumed 1 for the starting step. The optimized coefficients for the oxidation reaction were determined to be

$$\text{Spinel} + 0.07(O_2) \rightarrow 0.53\,(\text{Sesquioxide}) + 0.64\,(\text{Altered}\backslash, \text{Spinel}).$$

(8)
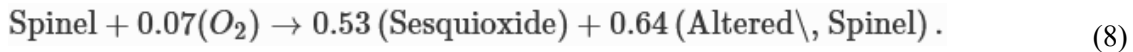
This optimization resulted in a R^2 value of 0.996 between product and reagent atoms when oxidation reactions of all 14 ores were considered and are representative of the average oxidation reaction observed at 1200 °C based on stoichiometry and the SEM–EDS analysis of the individual phases.

Statistical Relationships with Raw Spinel Compositions

To gain insight into the cations that influence the oxidation behavior, statistical relationships between the raw spinel compositions (as determined by SEM–EDS) and the observed oxidation behavior were explored. After assigning numerical values to the ore groupings observed in the TGA results (*i.e.*, 1, 2 and 3), the groupings were found to be most strongly correlated with the Cr:Al ratio of the starting spinel ($r = 0.84$, $P < 0.001$), this being the case despite the impact of

gangue constituents on the TGA. Due to the categorical nature of the groupings, exploratory data analysis was also performed using Orange v3.29.[73] In confirmation of the linear correlations, it was found that the spinels could be classified within the TGA groupings with an accuracy of 91.67 pct using only the initial Cr:Al ratio and a binary decision tree classification model.[74] The rules governing this classification model in a family of "if then" rules are summarized in Table X and correctly classify 11 of the 12 ores examined during the TG runs according to their mass change behavior during increasing temperature. Chromite ores with the lowest Cr:Al ratios were therefore observed to have the steepest percentage mass change vs temperature slopes and achieved greater increase in mass during oxidation.

Table X. Unraveled Classification Rules Governing Grouping of Investigated Spinels into Groupings Based on TG Behavior

Unraveled Rules	Attribute	Accuracy
If Cr:Al ≤ 1.902 then Group = 1	Cr:Al	5/5 = 100 pct
If Cr:Al > 1.902 and Cr:Al ≤ 1.974 then Group = 2	Cr:Al	3/3 = 100 pct
If Cr:Al > 1.902 and Cr:Al > 1.974 then Group = 3	Cr:Al	3/4 = 75 pct

The strongest positive correlation with the sesquioxide mass fraction, as determined by SEM–EDS, was determined to be the total Fe content of the spinel ($r = 0.93$, $P < 0.001$). The mass percent of sesquioxide phase formed (as determined using SEM–EDS) after oxidation at 1200 °C can be predicted with reasonable accuracy ($R^2 = 0.85$) based solely on the starting Fe content of the spinel, according to

$$\text{Pct} \, \text{Sesquioxide} = 195.6 n_{Fe} - 94.568, \tag{9}$$

where n_{Fe} is the molar fraction of Fe present in the raw spinel when the oxygen atoms are normalized to four. This confirms that the starting spinel composition does indeed need to be taken into consideration regarding the oxidative roasting behavior for application in SBS operations.

Industrial Samples

The results discussed thus far confirm that the sesquioxidation behavior of chromite spinels is influenced by the cation composition of the parent spinel, which is expected to influence the response to temperature as well as the amount of sesquioxide that can form during oxidation. The high levels of oxidation achieved for concentrates at 1200 °C, compared to the equilibrium amounts achievable calculated using FactSage, would suggest that the SBS operating temperatures should be adequate to achieve full oxidation. To test this hypothesis, pellets were sampled from a SBS currently in operation. The pellets were found to have poorly defined sesquioxide peaks, indicating incomplete oxidation. To determine if roasting temperature may have influenced the observed oxidation, the plant pellets were roasted for 10 minutes at 1200 °C in air in a muffle furnace. The diffraction patterns after roasting are compared with those of the as-received plant pellets in Figure 13 and show a substantial improvement in the formation of sesquioxide phase. Due to confidentiality the results cannot be fully disseminated, but this lends credibility to the hypothesis that variability in oxidation rate of SBS pellets could be contributing to the furnace performances observed. Further, this indicates that adequate temperature exposure could improve the sesquioxidation of SBS pellets.
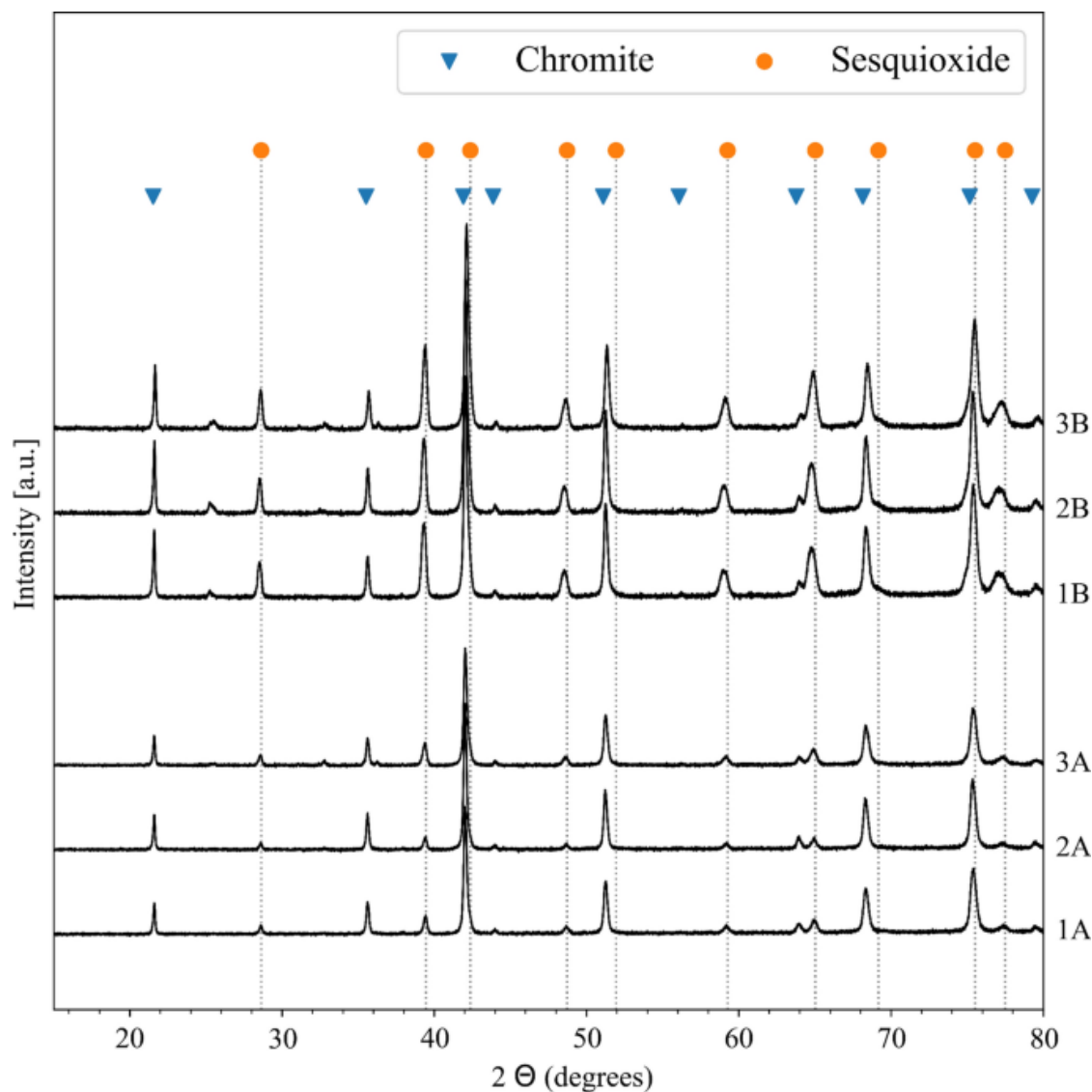
Fig. 13. XRD diffraction pattern for plant pellets as received (1A, 2A and 3A) and XRD patterns for the pellets after roasting (1B, 2B, 3B) at 1200 °C for 10 minutes showing a substantial increase in sesquioxide peaks

Conclusions

Fifteen concentrates used as feedstock for SBS operations were sampled, characterized, and studied after oxidative roasting in air at various temperatures and reaction times. The following conclusions were drawn:

The chromite concentrates were found to respond uniquely to oxidative roasting during TGA. The TG behavior of the ores could be consolidated into three groups, with distinct slopes for percentage mass change *vs* temperature curves as well as total mass gain achieved. The TGA behavior was also correlated with the starting spinel cation composition, with the initial Cr:Al ratio showing the strongest linear correlation ($r = 0.84$, $P < 0.001$) for the TGA groupings. It was possible to classify the ores with 91.67 pct accuracy using only the Cr:Al ratio using binary decision tree classification. The Cr:Al ratio of the starting spinel is concluded to be influential in determining the oxidizing behavior of the chromite ore.

33

The mass fraction of sesquioxide phase formed was evaluated by Rietveld refinement as well as with SEM–EDS-based calculations and the quantities determined by each method were found to be in good agreement. Diffusion kinetics and microstructural effects appear to prevent attainment of equilibrium conditions. The sesquioxide quantities after reaction, as determined by the SEM–EDS technique, were found to be most strongly correlated with the total Fe content ($r = 0.93$, $P < 0.001$) of the starting spinel.

With regard to the aims of the investigation, it was found that

a. South African chromite ores with a lower Cr:Al ratio had the steepest rate of mass gain during TG analysis, while the amount of sesquioxide that formed after firing at 1200 °C can be predicted by the initial total Fe content.
b. Counter-diffusion of Mg and Fe^{2+} cations was confirmed, while the slower diffusion rates of Cr and Al cations appear to be influential in determining how the sesquioxidation reaction progresses, with the Cr:Al ratio remaining largely constant across all the phases observed.
c. The slow diffusion rates of Cr and Al decrease the likelihood that free eskolaite will form as a precipitate, and indeed no evidence of free eskolaite formation could be found.
d. The low temperature (above 500 °C but below 800 °C) oxidation behavior, observed as mass gain during TGA, did not impart compositional changes that could be observed with the XRD or SEM techniques used.

Acknowledgments

Conflict of interest

The authors declare that they have no conflict of interest.

References

1. L. Holappa: in *Handbook of Ferroalloys: Theory and Technology*, 1st ed., M. Gasik, ed., Elsevier Science, Oxford, 2013, pp. 9–28.
2. ICDA: *Ferrochrome Q1 2021 Quarterly Industry Overview*, ICDA, 2021. https://www.icdacr.com/. Accessed 6 August 2021.
3. R. Fichte: in *Handbook of Extractive Metallurgy*, vol. III, F. Habashi, ed., Wiley-VCH, Weinheim, 1997, pp. 438–53.
4. R.T. Jones and M.W. Erwee: *CALPHAD*, 2016, vol. 55, pp. 20–25.
5. R. Urquhart: *Miner. Sci. Eng.*, 1972, vol. 4, pp. 48–65.
6. E. Ringdalen, M. Rocha, and P. Figueiredo: *Proc. 14th Int. Ferroalloys Conf.*, Kiev, Ukraine, 2015, pp. 668–75.
7. J.H. Zietsman, A. Steyn, and W. Pretorius: *Proc. 15th Int. Ferroalloys Conf.*, Cape Town, South Africa, 2018, pp. 1–27.
8. L.A. Cramer, J. Basson, and L.R. Nelson: *J. S. Afr. Inst. Min. Metall.*, 2004, vol. 104, pp. 517–27.

9. Outokumpu now Outotec: *Australian Mining*. https://www.australianmining.com.au/news/outokumpu-now-outotec/. Accessed 6 August 2021.

10. L. Hekkala, T. Fabritius, and J. Härkki: *Proc. 10th Int. Ferroalloys Conf.*, Cape Town, South Africa, 2004, pp. 585–92.

11. Miningreview.com, G.: *Metso Outotec Emerges from Merger*, Miningreview.com, 2020. https://www.miningreview.com/international/metso-outotec-emerges-from-merger/. Accessed 6 August 2021.

12. J. Daavittila, M. Honkaniemi, and P. Jokinen: *Proc. 10th Int. Ferroalloys Conf.*, Cape Town, South Africa, 2004, pp. 432–43.

13. R.J. Hill, J.R. Craig, and G.V. Gibbs: *Phys. Chem. Miner.*, 1979, vol. 4, pp. 317–39.

14. L.W. Fisher: *Am Mineral. J. Earth Planet. Mater.*, 1929, vol. 14, pp. 341–57.

15. Y.R. Murthy, S.K. Tripathy, and C.R. Kumar: *Miner. Eng.*, 2011, vol. 24, pp. 375–80.

16. K. Perry, C. Finn, and R. King: *Metall. Trans. B*, 1988, vol. 19, pp. 677–84.

17. V. Urusov: *Phys. Chem. Miner.*, 1983, vol. 9, pp. 1–5.

18. A. Hammarberg: Recovery of Valuable Metals or Metal Compounds from Complex Ores, United States Patent 2,123,240, 1938.

19. K. Konopicky and F. Caesar: *Ber. Dtsch. Keram. Ges.*, 1939, vol. 20, pp. 367–73.

20. N.E. Dobbins and W.J. Rees: *Special Report 32*, The Iron and Steel Institute, London, 1946, pp. 211–33.

21. J.R. Rait: *Third Report on Refractory Materials*, The Iron and Steel Inst. Spec. Rept. No. 32, 1946, pp. 175–209.

22. A. Lekatou and D. Walker: *Ironmak. Steelmak.*, 1995, vol. 22, pp. 227–38.

23. V.D. Tathavakar, M.P. Antony, and A. Jha: *Metall. Mater. Trans. B*, 2005, vol. 36B, pp. 75–84.

24. B. Zhao and P.C. Hayes: *Proc. 12th Int. Ferroalloys Conf.*, Helsinki, Finland, 2010, pp. 263–74.

25. J. Pan, C. Yang, and D. Zhu: *ISIJ Int.*, 2015, vol. 55, pp. 727–35.

26. Y. Xiao, M. Reuter, and L. Holappa: *Proc. 9th Int. Ferroalloys Conf.*, Quebec City, Canada, 2001, pp. 147–56.

27. M.H. Khedr: *ISIJ Int.*, 2000, vol. 40, pp. 309–14.

28. J.P. Beukes, N.F. Dawson, and P.G. Van Zyl: *J. S. Afr. Inst. Min. Metall.*, 2010, vol. 110, pp. 743–50.

29. G. Ramakrishna, A. Kadrolkar, and N. Gurulaxmi Srikakulapu: *Metall. Mater. Trans. B*, 2014, vol. 46B, pp. 1073–81.

30. Y. Yang, Y. Xiao, and M.A. Reuter: *Proc. 10th Int. Ferroalloys Conf.*, Cape Town, South Africa, 2004, pp. 15–25.

31. E. Ringdalen: PhD Thesis, NTNU, Norway, 1999.

32. L.J. Erasmus: *Proc. 7th Int. Ferroalloys Conf.*, Trondheim, Norway, 1995, pp. 273–85.

33. L.R. Nelson: *Celebr. Megascale: Proc. Extr. Process. Div. Symp. Pyrometall. Honor of David G.C. Robertson*, San Diego, California. 2014, pp. 39–68.

34. M.M. Langa, P.J. Jugo, M.I. Leybourne, D.F. Grobler, J. Adetunji, and H. Skogby: *Miner. Depos.*, 2021, vol. 56, pp. 31–44.

35. C.J. Penberthy and R.K.W. Merkle: *S. Afr. J. Geol.*, 1999, vol. 102, pp. 240–50.

36. G. Von Gruenewaldt, C.J. Hatton, and R.K.W. Merkle: *Econ. Geol.*, 1986, vol. 81, pp. 1067–79.

37. P.A. Wagner: *S. Afr. J. Sci.*, 1923, vol. 20, pp. 223–35.

38. C.R. Borra, G. Kapure, and V. Tathavadkar: *Tata Search*, 2010, vol. 1, pp. 145–48.

39. G. Kapure, V. Tathavadkar, C.B. Rao, S.M. Rao, and K.S. Raju: *Proc. 12th Int. Ferroalloys Conf.*, Helsinki, Finland, 2010, pp. 293–302.

40. A. Biswas, B. Konar, G.U. Kapure, N. Sahu, and M. Paliwal: *Miner. Process. Extr Metall.*, 2021, vol. 130, pp. 31–41.
41. D. Zhu, C. Yang, J. Pan, and X. Li: *Metall. Mater. Trans. B*, 2016, vol. 47B, pp. 2919–30.
42. D. Zhu, C. Yang, J. Pan, Q. Zhang, B. Shi, and F. Zhang: *Metall. Mater. Trans. B*, 2016, vol. 47B, pp. 1010–23.
43. E.L.J. Kleynhans, B.W. Neizel, J.P. Beukes, and P.G. Van Zyl: *Miner. Eng.*, 2016, vol. 92, pp. 114–24.
44. V. Tathavadkar, M. Antony, and A. Jha: *Scand. J. Metall.*, 2004, vol. 33, pp. 65–75.
45. M. Yildirim, D. Özyürek, and T. Tunçay: *High Temp. Mater. Process.*, 2017, vol. 36, pp. 515–21.
46. H. Rietveld: *Acta Crystallogr.*, 1967, vol. 22, pp. 151–52.
47. N. Doebelin and R. Kleeberg: *J. Appl. Crystallogr.*, 2015, vol. 48, pp. 1573–80.
48. A. Vaitkus, A. Merkys, and S. Gražulis: *J. Appl. Crystallogr*, 2021, vol. 54, pp. 661–72.
49. R.T. Downs and M. Hall-Wallace: *Am. Mineral.*, 2003, vol. 88, pp. 247–50.
50. C.W. Bale, E. Bélisle, P. Chartrand, S.A. Decterov, G. Eriksson, A.E. Gheribi, K. Hack, I.H. Jung, Y.B. Kang, J. Melançon, A.D. Pelton, S. Petersen, C. Robelin, J. Sangster, P. Spencer, and M.A. Van Ende: *CALPHAD*, 2016, vol. 54, pp. 35–53.
51. S.A. Degterov, A.D. Pelton, E. Jak, and P.C. Hayes: *Metall. Mater. Trans. B*, 2001, vol. 32B, pp. 643–57.
52. M. Hillert: *J. Alloys Compd.*, 2001, vol. 320, pp. 161–76.
53. Eastplats: *Eastern Platinum Limited Reports Successful PGM Production from Scavenger Circuit and Operational Update*, 18 Feb 2020. https://eastplats.com/eastern-platinum-limited-reports-successful-pgm-production-from-scavenger-circuit-and-operational-update/. Accessed 26 July 2021.
54. G.T.R. Droop: *Mineral. Mag.*, 1987, vol. 51, pp. 431–35.
55. P.B. Arab, T.P. Araújo, and O.J. Pejon: *Appl. Clay Sci.*, 2015, vol. 114, pp. 133–40.
56. M. Wesołowski: *Thermochim. Acta*, 1984, vol. 78, pp. 395–421.
57. B.Z. Dlugogorski and R.D. Balucan: *Renew. Sustain. Energy Rev.*, 2014, vol. 31, pp. 353–67.
58. D.D. Howat, P.R. Jochens, J.C. Payntcr, and N.A. Barcza: *Report No. 1365*, National Institute for Metallurgy, 1972.
59. N.A. Barcza: Master's Thesis, University of Witwatersrand, South Africa, 1971.
60. S. Sánchez-Ramos, A. Doménech-Carbó, J.V. Gimeno-Adelantado, J. Peris-Vicente, and F.M. Valle-Algarra: *Thermochim. Acta*, 2008, vol. 476, pp. 11–19.
61. L. Xing, Y. Qu, C. Wang, L. Shao, Z. Zou, and W. Song: *Metall. Mater. Trans. B*, 2020, vol. 51B, pp. 395–406.
62. J.M. Gallardo Amores, V. Sanchez Escribano, and G. Busca: *Mater. Chem. Phys.*, 1999, vol. 60, pp. 168–76.
63. I. Kondofersky, A. Müller, H.K. Dunn, A. Ivanova, G. Stefanic, M. Ehrensperger, C. Scheu, B.A. Parkinson, D. Fattakhova-Rohlfing, and T. Bein: *J. Am. Chem. Soc.*, 2016, vol. 138, pp. 1860–67.
64. J. Manjanna and G. Venkateswaran: *Ind. Eng. Chem. Res.*, 2002, vol. 41, pp. 3053–63.
65. R.E. Carter, W.L. Roth, and C.A. Julien: *J. Am. Ceram. Soc.*, 1959, vol. 42, pp. 533–36.
66. D. Hubble and N. Dodge: *Am. Ceram. Soc. Bull.*, 1961, vol. 40, pp. 498–502.
67. W.S. Treffner: *J. Am. Ceram. Soc.*, 1962, vol. 45, pp. 455–63.
68. G. Rigby, R. Hutton, and B. Hamilton: *J. Am. Ceram. Soc.*, 1963, vol. 46, pp. 332–42.

69. M.D. Abràmoff, P.J. Magalhães, and S.J. Ram: *Biophotonics Int.*, 2004, vol. 11, pp. 36–42.
70. A. Muan and S. Sömiya: *J. Am. Ceram. Soc.*, 1959, vol. 42, pp. 603–13.
71. A.M. Suzuki, A. Yasuda, and K. Ozawa: *Phys. Chem. Miner.*, 2008, vol. 35, pp. 433–45.
72. L. Chandrakantha: *Using Excel Solver in Optimization Problems*, Mathematics and Computer Science Department, John Jay College of Criminal Justice of CUNY, 2014, pp. 42–49.
73. J. Demšar, T. Curk, A. Erjavec, Č Gorup, T. Hočevar, M. Milutinovič, M. Možina, M. Polajnar, M. Toplak, and A. Starič: *J. Mach. Learn. Res.*, 2013, vol. 14, pp. 2349–53.
74. J. Talar: *Arch. Metall. Mater.*, 2007, vol. 52, pp. 239–50.